

## Large-Amplitude Mountain Wave Breaking over Greenland

JAMES D. DOYLE

*Naval Research Laboratory, Monterey, California*

MELVYN A. SHAPIRO

*NOAA/Office of Weather and Air Quality, Boulder, Colorado*

QINGFANG JIANG

*University Corporation for Atmospheric Research, Monterey, California*

DIANA L. BARTELS

*National Severe Storms Laboratory, Norman, Oklahoma*

(Manuscript received 1 October 2004, in final form 17 February 2005)

### ABSTRACT

A large-amplitude mountain wave generated by strong southwesterly flow over southern Greenland was observed during the Fronts and Atlantic Storm-Track Experiment (FASTEX) on 29 January 1997 by the NOAA G-IV research aircraft. Dropwindsondes deployed every 50 km and flight level data depict a vertically propagating large-amplitude wave with deep convectively unstable layers, potential temperature perturbations of 25 K that deformed the tropopause and lower stratosphere, and a vertical velocity maximum of nearly  $10 \text{ m s}^{-1}$  in the stratosphere. The wave breaking was associated with a large vertical flux of horizontal momentum and dominated by quasi-isotropic turbulence. The Coupled Ocean–Atmosphere Mesoscale Prediction System (COAMPS) nonhydrostatic model with four-nested grid meshes with a minimum resolution of 1.7 km accurately simulates the amplitude, location, and timing of the mountain wave and turbulent breakdown. Finescale low-velocity plumes that resemble wakelike structures emanate from highly dissipative turbulent regions of wave breaking in the lower stratosphere. Idealized adiabatic three-dimensional simulations suggest that steep terrain slopes increase the effective Rossby number of the relatively wide Greenland plateau, decrease the sensitivity of the wave characteristics to rotation, and ultimately increase the tendency for wave breaking. Linear theory and idealized simulations indicate that diabatic cooling within the boundary layer above the Greenland ice sheet augments the effective mountain height and increases the wave amplitude and potential for wave breaking for relatively wide obstacles such as Greenland.

### 1. Introduction

Mountain waves generated by stratified flow passing over a topographic barrier have a fundamental influence on the atmosphere on a variety of spatial scales ranging from turbulence and wave breaking associated with downslope windstorms to the aggregate effects of wave drag and fluxes on the momentum balance of the atmospheric general circulation and climate (e.g.,

see reviews in Smith 1989; Fritts and Alexander 2003). The stratified flow response to idealized two-dimensional obstacles (Durran 1986; Doyle et al. 2000) and three-dimensional terrain (Smolarkiewicz and Rotunno 1989; Ólafsson and Bougeault 1996, 1997) has been extensively addressed in the literature. In contrast, relatively few investigations have considered the flow response to realistic topography, particularly for large-scale mountains such as Greenland, the Antarctic Peninsula, and Tibetan Plateau that have the potential to have a significant impact on the circulation through the generation of large-amplitude mountain waves and planetary waves (e.g., Grose and Hoskins 1979; Smolarkiewicz et al. 2001).

---

*Corresponding author address:* James D. Doyle, Marine Meteorology Division, Naval Research Laboratory, 7 Grace Hopper Avenue, Monterey, CA 93943-5502.  
E-mail: doyle@nrlmry.navy.mil

Report Documentation Page				Form Approved OMB No. 0704-0188	
Public reporting burden for the collection of information is estimated to average 1 hour per response, including the time for reviewing instructions, searching existing data sources, gathering and maintaining the data needed, and completing and reviewing the collection of information. Send comments regarding this burden estimate or any other aspect of this collection of information, including suggestions for reducing this burden, to Washington Headquarters Services, Directorate for Information Operations and Reports, 1215 Jefferson Davis Highway, Suite 1204, Arlington VA 22202-4302. Respondents should be aware that notwithstanding any other provision of law, no person shall be subject to a penalty for failing to comply with a collection of information if it does not display a currently valid OMB control number.					
1. REPORT DATE <b>17 FEB 2005</b>		2. REPORT TYPE		3. DATES COVERED <b>00-00-2005 to 00-00-2005</b>	
4. TITLE AND SUBTITLE <b>Large-Amplitude Mountain Wave Breaking over Greenland</b>				5a. CONTRACT NUMBER	
				5b. GRANT NUMBER	
				5c. PROGRAM ELEMENT NUMBER	
6. AUTHOR(S)				5d. PROJECT NUMBER	
				5e. TASK NUMBER	
				5f. WORK UNIT NUMBER	
7. PERFORMING ORGANIZATION NAME(S) AND ADDRESS(ES) <b>Naval Research Laboratory, 7 Grace Hopper Ave., Stop 2, Monterey, CA, 93943-5502</b>				8. PERFORMING ORGANIZATION REPORT NUMBER	
9. SPONSORING/MONITORING AGENCY NAME(S) AND ADDRESS(ES)				10. SPONSOR/MONITOR'S ACRONYM(S)	
				11. SPONSOR/MONITOR'S REPORT NUMBER(S)	
12. DISTRIBUTION/AVAILABILITY STATEMENT <b>Approved for public release; distribution unlimited</b>					
13. SUPPLEMENTARY NOTES					
14. ABSTRACT <b>see report</b>					
15. SUBJECT TERMS					
16. SECURITY CLASSIFICATION OF:			17. LIMITATION OF ABSTRACT <b>Same as Report (SAR)</b>	18. NUMBER OF PAGES <b>21</b>	19a. NAME OF RESPONSIBLE PERSON
a. REPORT <b>unclassified</b>	b. ABSTRACT <b>unclassified</b>	c. THIS PAGE <b>unclassified</b>			

Vertically propagating mountain waves increase in amplitude with height because of decreasing air density (Hines 1960; Lindzen 1967) or reverse wind shear layers (Smith 1989; Shen and Lin 1999), either of which independently or synergistically may lead to wave steepening, overturning, and subsequent turbulent breakdown, particularly in the stratosphere or mesosphere (e.g., Bacmeister and Schoeberl 1989; Fritts and Alexander 2003). An increase in the atmospheric stability such as the transition across the tropopause can reduce the vertical wavelength and increase the potential for wave breaking (VanZandt and Fritts 1989). Additionally, mountain waves may overturn and break as they approach a critical level (Clark and Peltier 1984; Dörnbrack 1998), a level at which the wave phase speed is equivalent to the wind component projected along the horizontal wave vector. High-resolution three-dimensional studies of wave breaking associated with overturning of isentropic surfaces highlight the role of nonlinear interactions that occur in the transition to turbulence (e.g., Fritts et al. 1996). Mountain wave breaking has a significant influence on the atmosphere for a number of reasons that include the impact of orographic drag on the large-scale circulation (Bretherton 1969; Palmer et al. 1986); downslope windstorms (Peltier and Clark 1979; Durran 1986); vertical mixing of water vapor, aerosols, and chemical species (Dörnbrack and Dürbeck 1998); potential vorticity generation (Schär and Smith 1993) and associated upscale forcing (Thorpe et al. 1993; Aebischer and Schär 1998); and clear-air turbulence that poses an aviation hazard (Lilly 1978; Ralph et al. 1997; Clark et al. 2000).

Although there have been numerous observational studies documenting mountain wave characteristics (e.g., Shutts 1992; Vosper and Mobbs 1996; Doyle and Smith 2003), direct observations of mountain wave breaking are relatively rare. The in situ observations of the windstorm and wave breaking in the lee of the Front Range of the Rockies on 11 January 1972 (Lilly and Zipser 1972; Lilly 1978) still may be the most complete set of observations of large-amplitude mountain wave breaking to date. The establishment of the link between resonant mountain wave amplification positioned beneath upper-level wave breaking regions that contain “wave induced” critical levels and downslope windstorm and gravity wave drag enhancement was motivated in part by these observations (Peltier and Clark 1979). The downslope windstorm has been subsequently shown to be consistent with internal hydraulic theory based on theoretical considerations (Smith 1985) and numerical simulations (Durran 1986). Other more recent observational evidence of mountain wave breaking has been documented, for example,

above the Front Range of the Rockies (Clark et al. 2000), the Alps (Jiang and Doyle 2004), and the Welsh Mountains (Worthington 1998).

Many of the numerical studies reported upon in the literature have used two- and three-dimensional basic terrain shapes with idealized initial states to establish the characteristics of gravity wave breaking (e.g., Clark and Peltier 1984; Bacmeister and Schoeberl 1989; Ólafsson and Bougeault 1996, 1997; Epifanio and Durran 2001). There are relatively few studies that have used complex terrain and real-atmospheric initial states to simulate wave breaking. Examples include the Clark et al. (2000) study that used a high-resolution model to simulate a downslope windstorm and clear-air turbulence event over the Rockies and documented the generation of horizontal vortex tubes within wave breaking regions along a jet stream in the upper troposphere. Schmid and Dörnbrack (1999) simulated lower stratospheric wave breaking over the Alps associated with a critical level above the jet stream. Leutbecher and Volkert (2000) found that the simulation of mountain waves generated by Greenland were sensitive to the horizontal model resolution and surface friction representation. The multiscale terrain of the Alps was shown by Jiang and Doyle (2004) to promote wave breaking and increase wave drag. Although several of these previous real-data simulations have replicated the limited observations of the wave breaking evolution with reasonable accuracy, the predictability of wave breaking is not well established. For example, simulations of the 1972 Boulder windstorm using 11 different numerical models, all with identical initial states and two-dimensional terrain, exhibit diverse wave breaking evolution in some cases (Doyle et al. 2000). Outstanding issues regarding gravity wave breaking in the real atmosphere that are potentially important for mesoscale numerical weather prediction include turbulent mixing and wave overturning processes, mountain wave drag, downstream effects, and predictability of wave breaking. The current limit in our understanding of gravity wave breaking can be partially attributed to lack of observations.

During the Fronts and Atlantic Storm-Track Experiment (FASTEX) (Joly et al. 1997), a large-amplitude gravity wave was observed in the lee of Greenland on 29 January 1997 (e.g., see Doyle and Shapiro 1999). Data collected during FASTEX represents a unique opportunity to study topographically forced gravity wave breaking and to assess the ability of high-resolution numerical models to predict the structure and evolution of such phenomenon. The topography of Greenland (Fig. 1) is characterized by extremely steep terrain near the coastlines and an ice-covered plateau

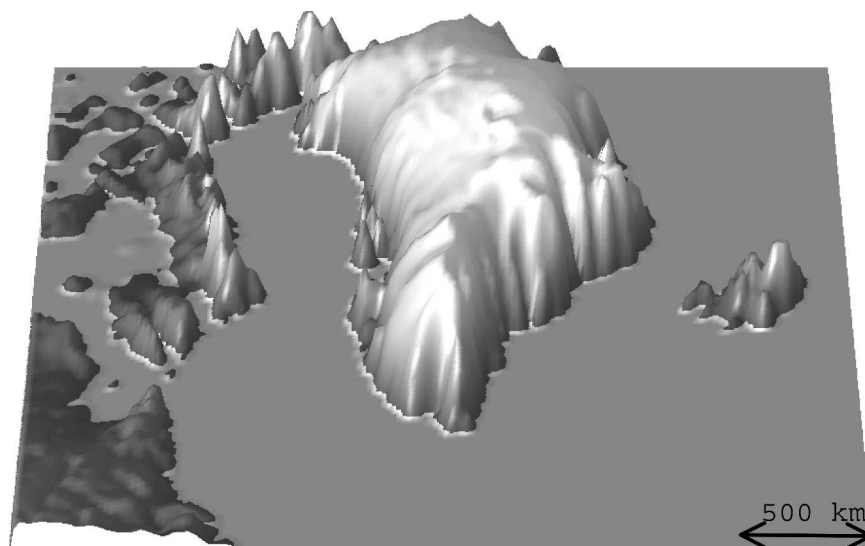


FIG. 1. Three-dimensional depiction of the Greenland relief.

exceeding 3000 m with an average ice thickness of 1790 m and a thickness maximum of 3400 m (Dolgushin and Osipova 1989). The terrain of Greenland is complex and characterized by a spectrum of mountain shapes ranging from half-widths of less than 150 km in the south to greater than 500 km in the central portion. The study of flow impinging on Greenland and the generation of mountain waves is important for a variety of reasons that include its formidable topography and ice sheet, the proximity to the semipermanent Icelandic cyclone (Petersen et al. 2003), influence on synoptic-scale systems (Schwierz and Davies 2003), polar stratospheric cloud generation (Chan et al. 1993), katabatic winds (Bromwich et al. 2001), clear-air turbulence (Lester et al. 1989) and wave breaking (Leutbecher and Volkert 2000), contribution to large-scale mountain torque (Wei and Schaack 1984), tip jets and associated high-latitude air–sea interaction processes (Doyle and Shapiro 1999; Pickart et al. 2003), and the emerging significance of Greenland for the climate system (Murphy et al. 2002).

In the present study, a nonhydrostatic model simulation is evaluated with continuous research aircraft and dropwindsonde observations from the National Oceanic and Atmospheric Administration (NOAA) G-IV aircraft. Real data and idealized model simulations are used to document the evolution, characteristics, and dynamics of the breaking gravity wave event. An overview of the numerical model is presented in section 2. The observations of the wave breaking event are discussed in section 3. The results from a series of numerical simulations performed with real data and idealized flows are presented in section 4. The relationship be-

tween diabatic cooling within the boundary layer and wave amplitude is explored in section 5. Section 6 contains the summary and conclusions.

## 2. Numerical model description

The atmospheric portion of the U. S. Naval Research Laboratory's Coupled Ocean–Atmosphere Mesoscale Prediction System (COAMPS; Hodur 1997) is utilized for the numerical simulations of observed and idealized flows in this study. COAMPS is based on a finite-difference approximation to the fully compressible, nonhydrostatic equations and uses a terrain-following vertical coordinate transformation. In this application, the finite difference schemes are of second-order accuracy in time and space. The compressible equations are integrated efficiently using a time splitting technique with a semi-implicit formulation for the vertical acoustic modes (Klemp and Wilhelmson 1978).

The planetary boundary layer and free-atmospheric turbulent mixing and diffusion are represented using a prognostic equation for the turbulence kinetic energy (TKE) budget for both real data and idealized simulations. The surface fluxes are computed following the Louis (1979) formulation, which makes use of a surface energy budget based on the force–restore method. The subgrid-scale moist convective processes are parameterized using an approach following Kain and Fritsch (1993). The grid-scale evolution of the moist processes are explicitly predicted from budget equations for cloud water, cloud ice, raindrops, snowflakes, and water vapor (Rutledge and Hobbs 1983). The shortwave and longwave radiation processes are parameterized follow-

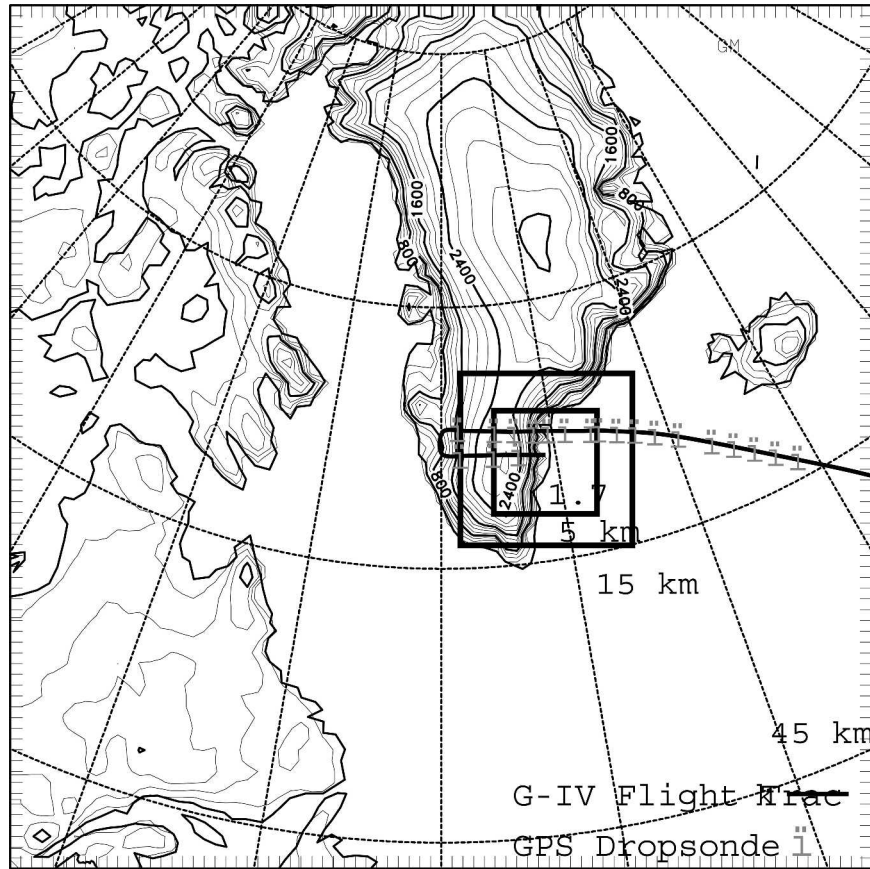


FIG. 2. The outer-grid mesh ( $\Delta x = 45$  km) topography and inner-grid mesh locations for the numerical simulation. The contour interval is 200 m. The NOAA G-IV flight track and dropsonde locations are indicated by the solid line and gray circles, respectively.

ing Harshvardhan et al. (1987). The real-data simulations use the full suite of physical parameterizations. For simplicity, the idealized simulations are adiabatic with a free-slip lower boundary condition and include free-atmosphere vertical diffusion derived from the explicitly predicted TKE.

The real-data simulations are initialized using an incremental update data assimilation procedure that enables mesoscale phenomena to be retained in the analysis increment fields (Barker 1992). The initial fields for the model are created from multivariate optimum interpolation analyses of upper-air sounding, surface, commercial aircraft, and satellite data that are quality controlled and blended with the 12-h COAMPS forecast fields. Lateral boundary conditions for the outermost grid mesh are derived from the U. S. Navy Operational Global Analysis and Prediction System (NOGAPS) forecast fields.

The domain configuration for the real-data simulations, as shown in Fig. 2, contains four horizontally nested grid meshes of  $81 \times 81$ ,  $73 \times 73$ ,  $133 \times 133$ , and

$223 \times 223$  points with horizontal grid increments on the computational meshes of 45 km, 15 km, 5 km, and 1.7 km, respectively. The model contains 80 vertical levels on a nonuniform vertical grid consisting of an increment of 10 m at the lowest level that gradually increases to 250 m at 12 km, 1000 m at 18 km, and continues with a 1000-m increment to the model top at 30 km. A radiation upper boundary condition is applied to mitigate the reflection of vertically propagating gravity waves. The topographic data for the simulations are based on the Global Land One-kilometer Base Elevation (GLOBE) dataset, made available by NOAA National Geophysical Data Center, which enables orographic characteristics, such as steep slopes of the Greenland ice sheet and the complex coastal orography, to be well represented, as shown in Figs. 1 and 2.

### 3. Observations

Several different sources of observations are used to describe the synoptic-scale and mesoscale atmospheric



conditions on 29 January 1997, as well as the mountain waves over Greenland. This set of observations includes the routine radiosondes, satellite imagery, and research aircraft measurements that include continuous flight level data and Global Positioning System (GPS) dropwindsondes.

#### a. Synoptic-scale flow

A broad region of deep southwesterly flow extended from eastern Canada to northeast of Greenland, as illustrated by the COAMPS 12-h forecast of wind speed at 700-, 500-, and 250-hPa levels valid at 1200 UTC 29 January 1997 (Fig. 3). Synoptic-scale features of interest include a shortwave trough positioned over eastern Canada, a shortwave ridge located upstream and to the southwest of Greenland, and an upper-level front and deformation zone situated near Iceland. The southwesterly flow was strongest over the southern one-third of Greenland with winds upstream of Greenland attaining speeds from  $7.5$  to  $15 \text{ m s}^{-1}$  at 700 hPa (Fig. 3a) and  $15$  to  $30 \text{ m s}^{-1}$  at 500 hPa (Fig. 3b). At higher latitudes north of  $70^\circ\text{N}$ , there is relatively weak flow across the Greenland topography. The relatively strong southwesterly flow upstream of Greenland is confirmed by the radiosonde and dropwindsonde observations along western and southern Greenland shown in Figs. 3a,b. The relatively small vertical shear of the horizontal wind direction, as indicated by the 700- and 250-hPa winds (Figs. 3a,c), was conducive for deep propagation of gravity waves due to the lack of directional critical levels (e.g., Shutts 1998).

The visible satellite image from *NOAA-12* valid at 1446 UTC 29 January, shown in Fig. 4, indicates that a southwest–northeast oriented band of lower- and middle-level clouds was present near Iceland, associated with the synoptic-scale baroclinic system. A broad region of lower- and middle-level clouds was present upstream of Greenland and a clear region was evident to the east, indicative of flow descent. Figure 5 presents the surface wind speeds at 1431 UTC 29 January 1997 derived from Special Sensor Microwave Imager (SSM/I) with an effective resolution of  $25 \text{ km}$  and rmse of  $\sim 5 \text{ m s}^{-1}$ . The SSM/I winds indicate that a swath of surface wind speeds were in excess of  $20 \text{ m s}^{-1}$  upstream of Greenland. A weak region of wind speed with a minimum of approximately  $5 \text{ m s}^{-1}$  was present in the lee of Greenland along the eastern shore consistent with surface properties of a large-scale wake (e.g., Pan and Smith 1999; Doyle and Shapiro 1999; Petersen et al. 2003).

Radiosonde soundings taken at the southern tip of Greenland at Narssarsuaq, valid at 0000 and 1200 UTC 29 January 1997, are shown in Figs. 6a and 6b. At

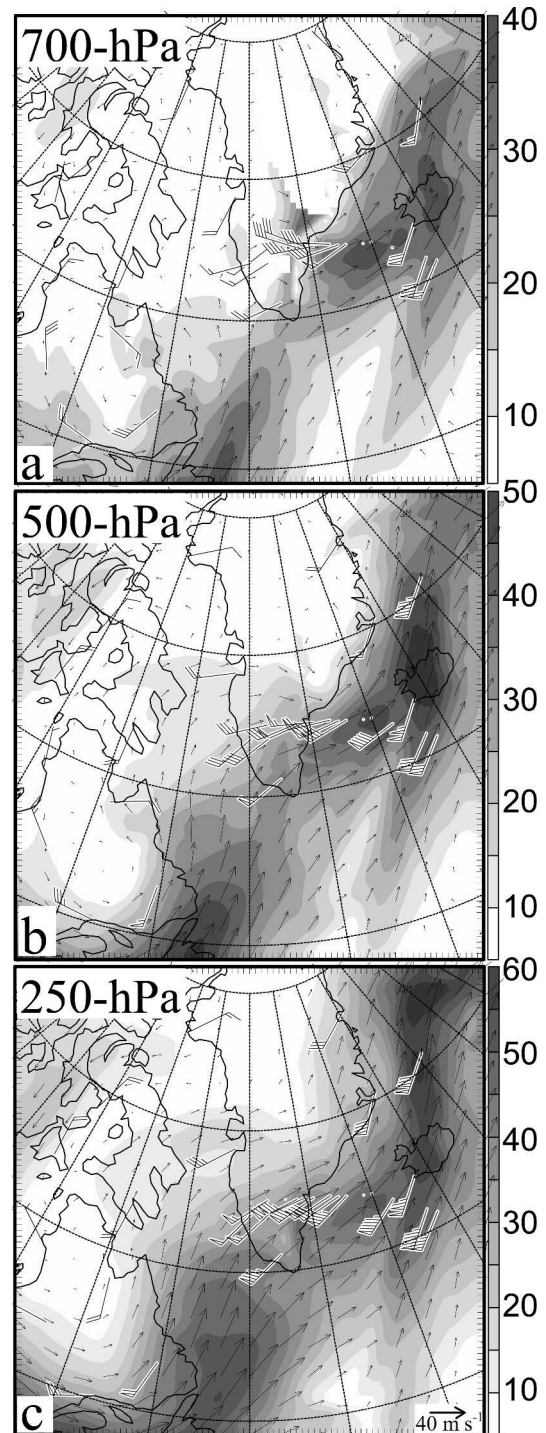


FIG. 3. The 12-h simulated wind speed (grayscale every  $5 \text{ m s}^{-1}$ ) valid at 1200 UTC 29 Jan 1997 for (a) 700, (b) 500, and (c) 250 hPa. Radiosonde and dropwindsonde winds are shown by the station model wind vectors with full and half bars representing  $5$  and  $2.5 \text{ m s}^{-1}$ , respectively, and a pennant  $25 \text{ m s}^{-1}$ .

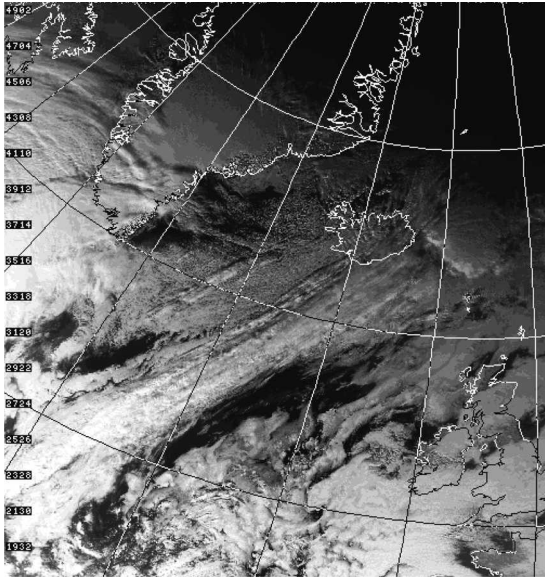


FIG. 4. The NOAA-12 visible satellite image valid at 1446 UTC 29 Jan 1997 (obtained from the University of Dundee).

0000 UTC 29 January, relative strong westerlies are present in the 850–500-hPa layer with wind speeds exceeding  $20 \text{ m s}^{-1}$  at 500 hPa. The layer between the surface and 5 km is characterized by a relatively strong static stability, corresponding to a Brunt–Väisälä frequency,  $N$ , of  $\sim 0.013 \text{ s}^{-1}$ , similar to the stability in the 5–8.5 km layer that contains a mean  $N$  of  $\sim 0.015 \text{ s}^{-1}$ . A

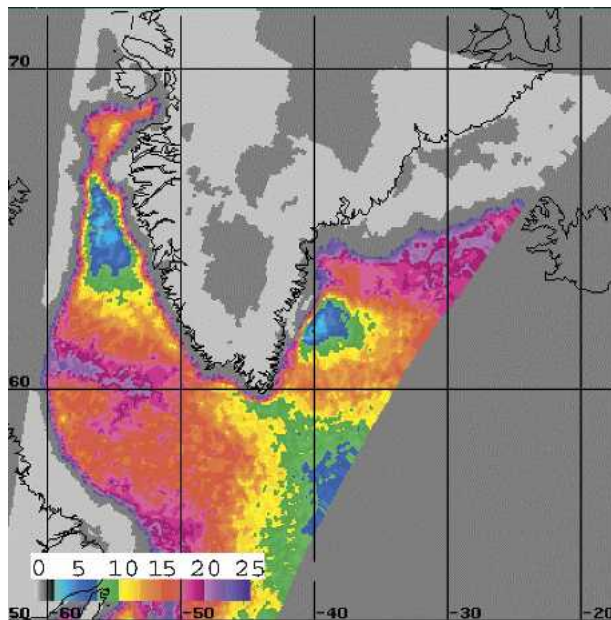


FIG. 5. Near-surface wind speed derived from SSM/I for 1431 UTC 29 Jan 1997. The wind speed is represented by the color scale ( $\text{m s}^{-1}$ ).

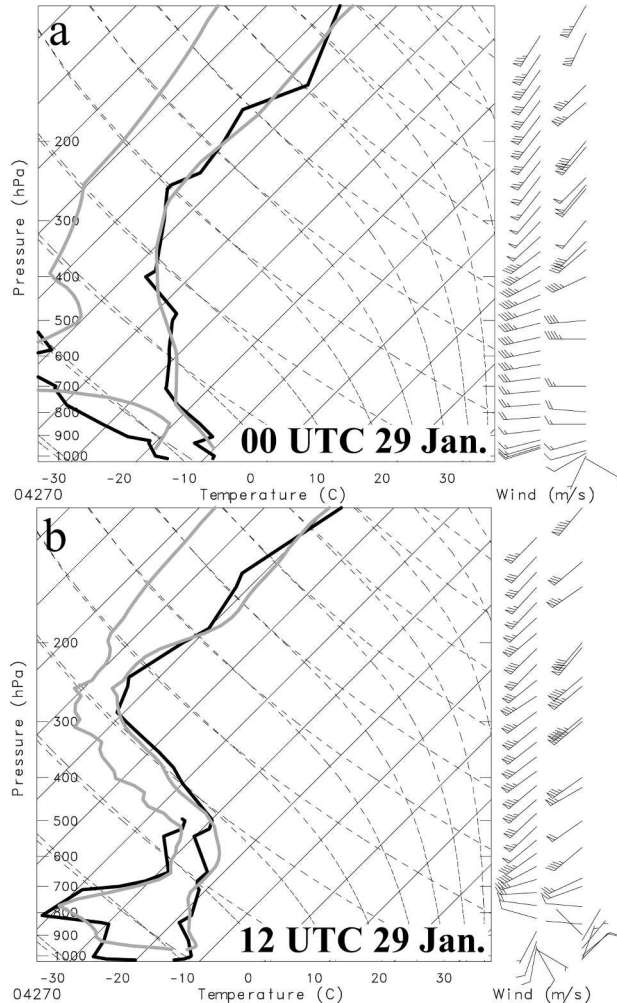


FIG. 6. Skew  $T$ -log  $p$  diagram (temperature, dewpoint, and wind profiles) for Narssarssuaq, Greenland (solid black soundings), valid at (a) 0000 and (b) 1200 UTC 29 Jan 1997. The model soundings are shown by the gray lines. The wind speeds ( $\text{m s}^{-1}$ ) from the model (right) and radiosonde (far right) are shown along the right side of the diagram with full and half barbs representing 5 and  $2.5 \text{ m s}^{-1}$ , respectively, and a pennant  $25 \text{ m s}^{-1}$ .

marked change in the tropospheric stratification and winds occurs in the following 12-h period such that a three-layer stratification develops by 1200 UTC 29 January (Fig. 6b). A strong stable layer, which contains several shallow inversions, is present below 5 km ( $\sim 500$  hPa) and has a corresponding mean  $N$  of  $\sim 0.015 \text{ s}^{-1}$ . The 500–300-hPa layer is characterized by a much weaker stability,  $N \sim 0.008 \text{ s}^{-1}$ , relative to the more stable lower troposphere and lower stratosphere. In the lowest 2 km, the flow is weak with a pronounced vertical speed shear in the 2–3-km layer. Observed wind speeds range from  $12 \text{ m s}^{-1}$  at 700 hPa, which is near the maximum height of the southern Greenland topog-



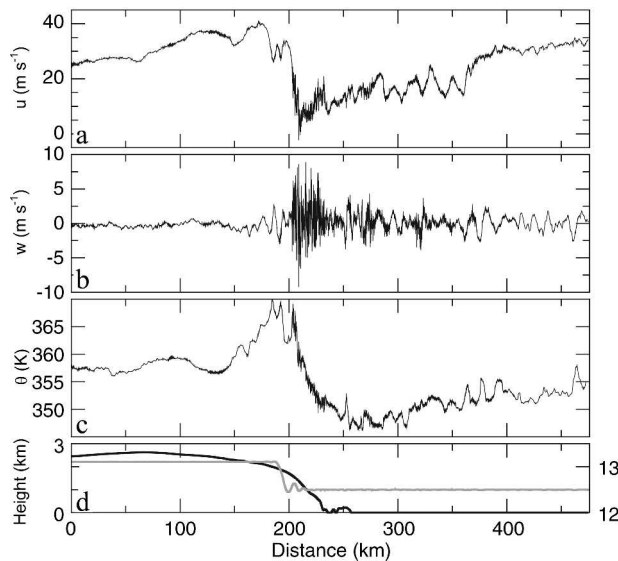


FIG. 7. The NOAA G-IV 25-Hz flight level (180 hPa or  $\sim 12$  km) measurements of the (a) horizontal velocity ( $\text{m s}^{-1}$ ), (b) vertical velocity ( $\text{m s}^{-1}$ ), and (c) potential temperature (K) for a portion of the flight path that extended from central Greenland to 150 km offshore. (d) The terrain height (km) (black, left axis) interpolated to the flight path and aircraft altitude (km) (gray, right axis).

raphy, to  $30 \text{ m s}^{-1}$  at 500 hPa and further increasing to  $49 \text{ m s}^{-1}$  near the tropopause level.

#### b. Research aircraft measurements

Measurements from the NOAA G-IV research aircraft were used to document the evolution and dynamics of a large-amplitude gravity wave event over Greenland, which also provide mesoscale observational validation data for the numerical simulations. During the research flight, 20 dropwindsondes were deployed along the flight path from an altitude of approximate 12 km (Fig. 2). The flight path was oriented in an east-west direction approximately along the large-scale wind direction and spanned across the entire Greenland ice shelf at  $\sim 64.5^\circ\text{N}$ . The in situ 25-Hz flight level ( $\sim 180$  hPa or 12 km)  $u$  wind component, vertical velocity, and potential temperature are shown in Fig. 7 for the section of the flight path between  $46^\circ$  and  $36^\circ\text{W}$ . A large-amplitude wave signature with a horizontal scale in excess of 200 km is apparent in the  $u$  wind component (Fig. 7a), and the potential temperature (Fig. 7c) above the steep eastern slope of the Greenland ice sheet. The wave breaking is associated with horizontal shear of the cross-mountain wind component in excess of  $10^{-3} \text{ s}^{-1}$  and a 25-K potential temperature perturbation across the large-scale wave. The wind speed downstream of the breaking wave decreases by  $30 \text{ m s}^{-1}$ , resulting in

the reduction of the cross-mountain flow to near zero with localized flow reversal regions. The maximum vertical velocity magnitude approaches  $\sim 10 \text{ m s}^{-1}$  during the turbulent episode associated with the wave breaking (Fig. 7b). Gravity wave activity characterized by shorter horizontal wavelengths (less than 15 km) is evident in the velocity and potential temperature fields downstream of the prominent larger-scale wave breaking signature and extends to a distance of over 150 km. Due to the encounter with the extreme turbulence, the research aircraft ascended from 12.5 to 13.1 km ASL (Fig. 7d).

Manual vertical cross-section analysis of continuous flight level and dropwindsonde data, with a 50-km horizontal spacing, document the presence of the large-amplitude breaking gravity wave that extends from the 12-km level downward to 5 km ASL (Fig. 8a). Analysis of dropwindsondes 15 and 16 and the in situ flight level data suggest that phase lines tilt upshear with height in the upper portion of the wave similar to that of mountain waves in the hydrostatic regime (e.g., Smith 1989). The dropsonde spacing is insufficient to conclusively deduce the tilt of the phase lines in the lower portion of the wave, such as in the 3–6-km layer, where the analysis indicates the phase lines tilt somewhat downstream with height. Convectively unstable layers of depths greater than 2 km were measured by dropwindsonde 15 above the steep leeside slope, suggestive of wave breaking and associated isentropic overturning. The cross-mountain wind component analysis (Fig. 8b) indicates a wind speed maximum near the lower portion of the mountain wave at 7.5 km ASL and a region of weak and reversed flow near the flight level at 12 km ASL, once again consistent with wave breaking. A wind speed maximum greater than  $28 \text{ m s}^{-1}$  is positioned near the surface along the steep lee slope. The strong near-surface downslope winds rapidly transition to weak flow in the lee coincident with abruptly ascending isentropes, which is consistent with a hydraulic-like flow response (e.g., Durran 1986).

#### c. Wave breaking characteristics

To illustrate some of the characteristics of the wave breaking episode, TKE, momentum flux, and heat flux were computed from the research aircraft flight level data and are shown in Fig. 9. In these calculations, the perturbation fields are separated into scales less than 5 km, which is referred to as turbulence scale, and scales larger than 5 km, referred to as wave scale. The turbulence-scale perturbations are defined as:  $A' = A - \langle A \rangle$ , where angle brackets represent a moving average over 5 km. The wave-scale perturbations are derived using



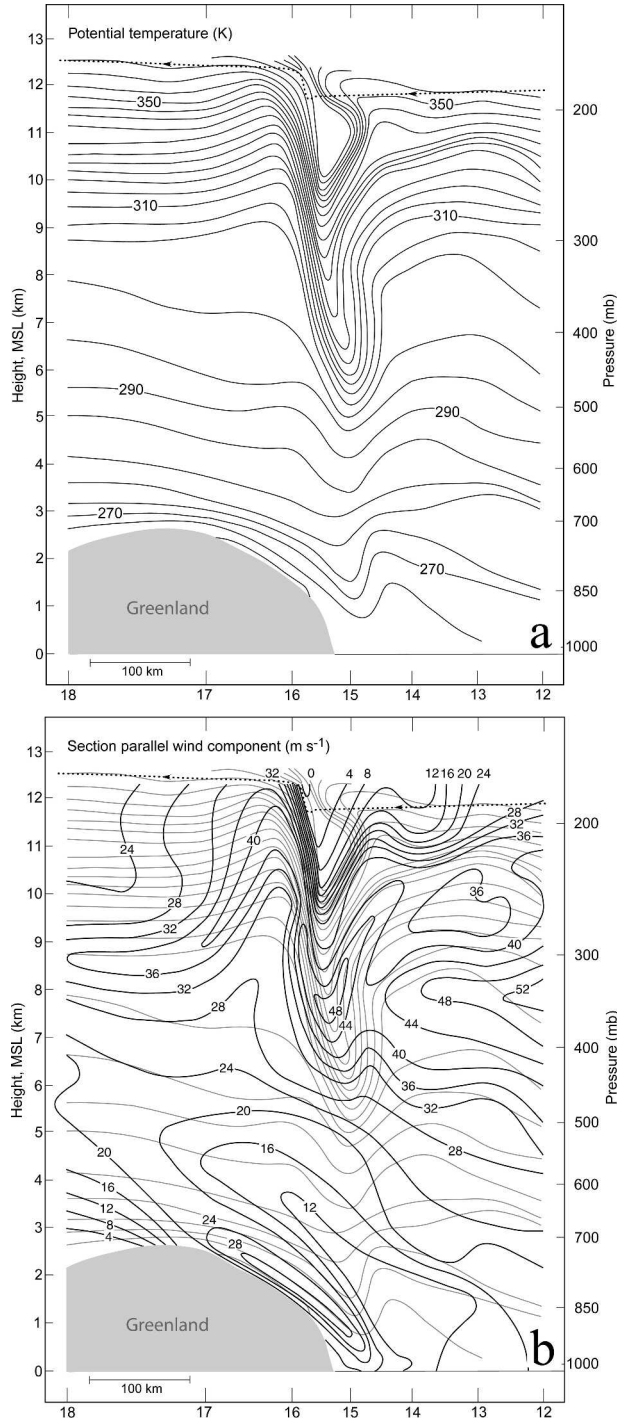


FIG. 8. Vertical cross-section analyses based on the NOAA G-IV in situ and dropwindsonde observations for (a) potential temperature (K) (isentrope interval 4 K) and (b) section-parallel wind speed ( $\text{m s}^{-1}$ ) (black, isotach interval  $4 \text{ m s}^{-1}$ ) and isentropes (gray) valid at 1200 UTC 29 Jan 1997.

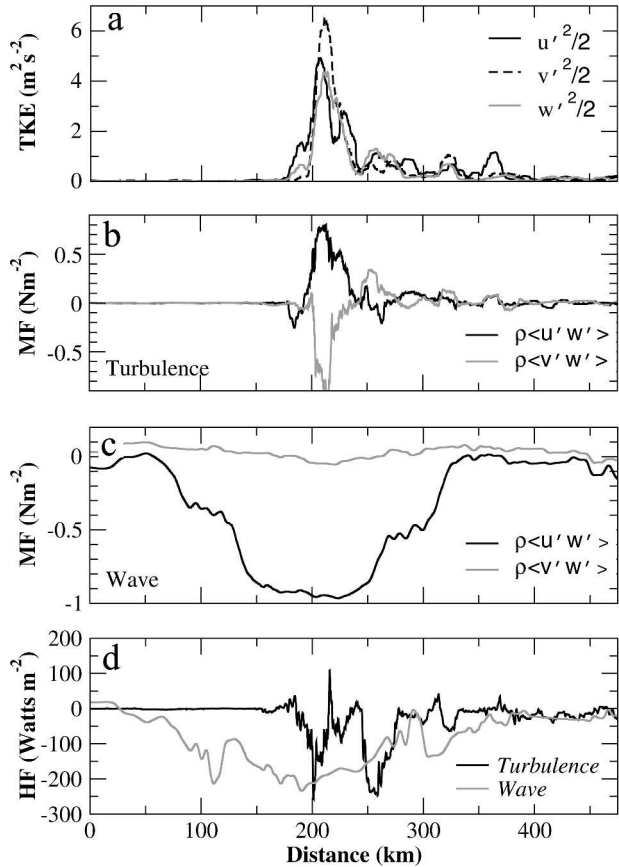


FIG. 9. Diagnostics derived from the NOAA G-IV 25-Hz flight level measurements consisting of (a) turbulence kinetic energy components, (b) vertical flux of horizontal momentum for the turbulence scales (less than 5 km), (c) vertical flux of horizontal momentum for the wave scale (greater than 5 km), and (d) vertical heat flux for turbulence and wave scales. The computations are performed along the identical segment as shown in Fig. 7.

$A' = \langle A \rangle - \langle \langle A \rangle \rangle$ , where the second-level average is computed over a 200-km length scale.

The TKE derived from the research aircraft data (Fig. 9a) indicates that an approximately 50-km wide maximum exists in the wave breaking zone with a long tail extending more than 180 km downstream, likely due to contributions from advection and local production. The TKE is displayed in Fig. 9a for each component,  $u'^2/2$ ,  $v'^2/2$ , and  $w'^2/2$ , where  $u$ ,  $v$ , and  $w$  are the zonal, meridional, and vertical wind components, respectively. The magnitudes of the three TKE components are comparable, indicative of quasi-isotropic turbulence.

The vertical flux of the horizontal momentum is shown in Figs. 9b,c. The portion of the vertical flux of the zonal momentum,  $\rho \langle u'w' \rangle$ , associated with turbulence-scale mixing is positive in the wave breaking zone, and the corresponding meridional flux,  $\rho \langle v'w' \rangle$ , is negative, where  $\rho$  is the air density. The zonal momen-

tum flux due to wave-scale perturbations is negative and similar to the horizontal scale of the gravity wave. The signature in the momentum flux is consistent with the characteristics of the large-amplitude wave. The meridional momentum flux is comparatively small.

The in situ research aircraft data is used to compute the vertical heat flux,  $C_p \rho \langle \theta' w' \rangle$ , where  $C_p$  is the specific heat capacity at constant pressure. The vertical heat flux associated with turbulence-scale perturbations, shown in Fig. 9d, indicates two major negative peaks within and downstream of the large TKE zone. If we assume that the mixing of heat is downgradient as well, the negative fluxes suggest that the layer is statically stable in the turbulence zone, which would limit turbulence production. In a recent study, Jiang and Doyle (2004) analyzed aircraft in situ measurements over a turbulent wave breaking zone in the middle troposphere in the central Alps. In the first flight transect analyzed in the Alpine study, the turbulence was nonisotropic and heat flux was positive, suggestive of turbulence in a development phase. During the second leg, the turbulence became near isotropic and the heat flux became negative, indicative of decaying turbulence. The characteristics of the turbulence measured by the research aircraft in this study was similar to that observed during the second flight leg in Jiang and Doyle. Thus, the turbulence may have been in a decay phase at the time of observation, although beneath the flight level turbulence production may be still active as indicated by the superadiabatic zone revealed by GPS dropsonde analysis. For a linear gravity wave, potential temperature and the vertical wind component should be in quadrature with zero heat flux averaged over one horizontal wavelength. In this case, the wave-scale vertical heat flux shows a large-scale negative maximum or downward heat flux in the region of the observed gravity wave, which may be due to nonlinearities in the wave breaking region.

The characteristics of the turbulence in the wave breaking zone measured by the research aircraft are further illustrated in Fig. 10 by the power spectrum in frequency and wavelength of the vertical velocity for 1140–1220 UTC 29 January, which is the time period that encompasses the wave breaking episode. The major peak in the vertical velocity spectrum, which occurs at a  $\sim 10$  km wavelength, is a manifestation of the shorter-scale waves evident in the vertical velocity observations upstream and downstream of the most intense breaking region (Fig. 7). These short-wavelength features are likely associated with the nonlinear breaking processes rather than a reflection of the dominant wavelength of the terrain (wavelength of the topography is approximately 300 km), which is clearly larger

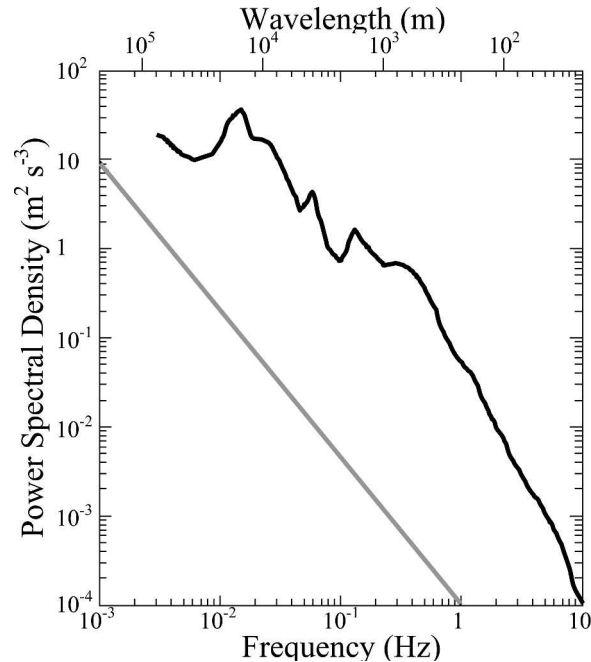


FIG. 10. Power spectrum in frequency and wavelength of the vertical velocity for the wave breaking episode (1140–1220 UTC 29 Jan). The  $k^{-5/3}$  slope is shown by the gray line.

than this spectral peak. Additional peaks in the spectrum occur at  $\sim 1$ – $5$  km wavelengths, which may be indicative of vigorous mixing dominated by large eddies consistent with a deep layer of isentropic overturning associated with large-amplitude wave breaking (Fig. 8a). At wavelengths less than approximately 1 km, an approximate slope of 2.7 to the energy spectrum is apparent, which deviates somewhat from the  $k^{-5/3}$  slope found in a number of studies including kinetic energy spectra derived from aircraft measurements (Nastrom and Gage 1985) and spectra derived from a B-57 aircraft during penetration of a region of severe turbulence (Lilly and Kennedy 1973). The velocity spectrum of the  $u$  wind component is dominated by a  $k^{-5/3}$  slope for the high-frequency portion.

#### 4. Numerical simulations of mountain wave breaking

High-resolution numerical simulations of the 29 January 1997 mountain wave breaking event were conducted using the COAMPS model with the objectives of assessing the ability of an operational modeling system to forecast wave breaking and documenting the characteristics and dynamics of the mountain wave evolution and breaking. Additional simulations were conducted using synthetic initial conditions in order to gain

insight into the relationship between the wave breaking and steep terrain.

*a. Numerical simulations of 29 January 1997 wave breaking event*

To accurately simulate mountain waves generated by complex terrain, the large-scale flow must be realistically represented because of the sensitivity of gravity wave characteristics, such as the amplitude and wavelength, to the upstream wind and stability profiles (e.g., Durran 1986; Smith 1989). The COAMPS simulated wind field on the 45-km resolution mesh, valid at 1200 UTC 29 January (12-h simulation time), agrees reasonably well with the radiosonde and GPS dropwindsonde observations for 700, 500, and 250 hPa, as shown in Figs. 3a–c. The relatively strong southwesterly flow over Greenland in the lower and middle troposphere are in agreement with the wind observations. The simulated winds are weakest over northern Greenland and strongest near the southern tip, also in agreement with the observations. The radiosonde and model-derived (based on the 15-km resolution mesh) soundings at Narssarssuaq for 0000 and 1200 UTC 29 January, are shown in Figs. 6a and 6b. The model-derived sounding at the initialization time, 0000 UTC 29 January, agrees well with the radiosonde. The profiles indicate that the model captures the increase of the lower-tropospheric static stability and decrease of the upper-level stability over the 12-h time period with reasonable skill. The simulated wind speed maximum near 300 hPa at 1200 UTC 29 January is  $\sim 40 \text{ m s}^{-1}$ , in contrast to the observed wind speed maximum of  $49 \text{ m s}^{-1}$ . Several of the smaller-scale structures in the sounding including shallow inversions are not particularly well represented; however, the model does capture the overall stability and wind profiles accurately.

Vertical cross sections of potential temperature and cross-mountain wind speed, based on the 5-km resolution mesh and oriented along a portion of the research aircraft transect, are shown in Figs. 11a and 11b, valid at 1000 UTC 29 January (10-h simulation time). The simulated upper-level wave breaking, as diagnosed by the region with TKE in excess of  $5 \text{ m}^2 \text{ s}^{-2}$ , vertically spans the 8–11-km layer above the lee slope and extends  $\sim 100 \text{ km}$  downstream (Fig. 11a). The isentropic cross section has a number of characteristics in common with the analysis based on the observations (Fig. 8a), which includes the weak stability layer in the upper troposphere and the deformed tropopause associated with the wave amplification and breaking. However, the simulation differs from the analysis in several respects. One primary difference is that the simulated wave amplitude and breaking region has a considerably

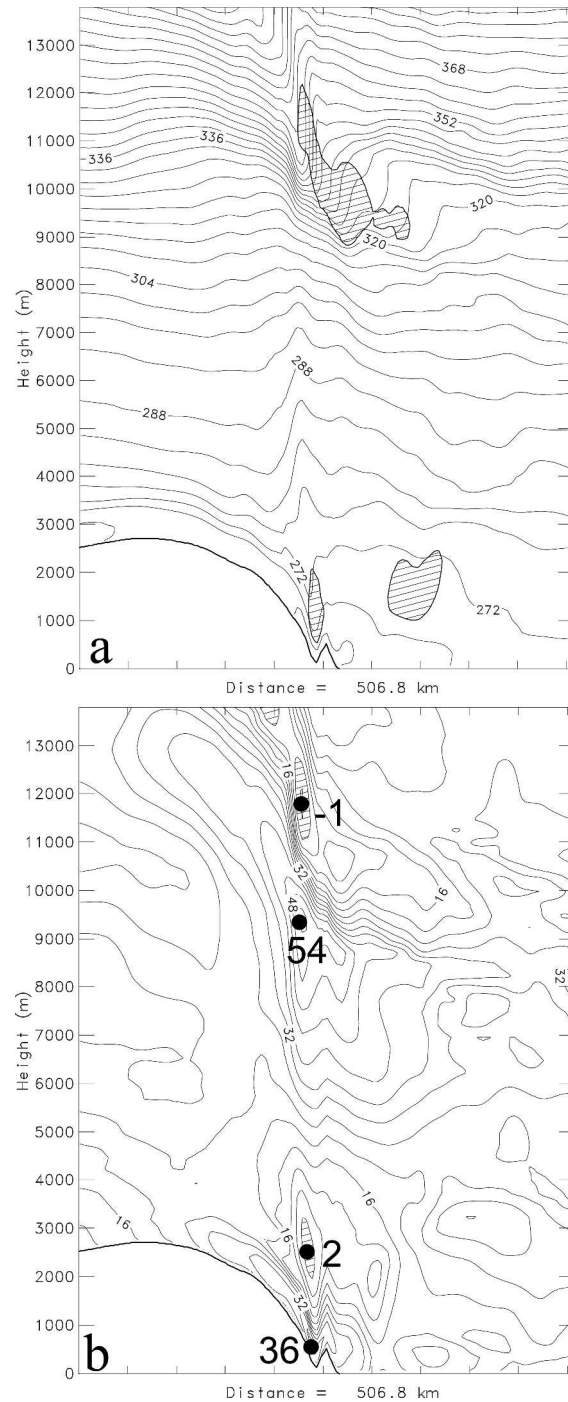


FIG. 11. Vertical cross sections derived from the COAMPS grid mesh 3 ( $\Delta x = 5 \text{ km}$ ) simulation for (a) potential temperature (K) (isentropic interval 4 K) with turbulent kinetic energy greater than  $5 \text{ m}^2 \text{ s}^{-2}$  hatched and (b) section parallel wind speed ( $\text{m s}^{-1}$ ) (isochore interval  $4 \text{ m s}^{-1}$ ) with regions of wind speed less than  $4 \text{ m s}^{-1}$  hatched. The cross sections are valid at 1000 UTC 29 Jan 1997 (10-h simulation time). The tick marks along the abscissa are shown every 50 km.



smaller amplitude than indicated by the dropsonde analysis. The analysis contains a layer of weaker static stability layer in the middle and upper troposphere upstream of the Greenland crest relative to the simulation. The implication of this static stability difference is that the simulated hydrostatic vertical wavelength,  $2\pi U/N$ , may be underestimated. The mean stability between mountaintop level (i.e., 3000 m) and wave breaking level ( $\sim 9000$  m), estimated using dropsonde 18 and the 1200 UTC COAMPS simulation time at the same location, is  $0.0139$  and  $0.0141 \text{ s}^{-1}$ , respectively. Since the static stability differences are rather small over the 3–9-km layer depth, the hydrostatic vertical wavelengths are nearly identical: 11.3 km based on the dropsonde and 11.1 km for the simulation. The static stability differences in the 5–9-km layer are somewhat greater, which implies a larger vertical wavelength based on the observations relative to the simulation. The differences in the upstream profiles apparently do not completely explain the nature of the discrepancy between the simulated and observed wave amplitude. Other factors that may impact the wave amplitude include vertical shear, nonlinearities, and baroclinicity. It is also noteworthy that the phase lines of the simulated vertically propagating waves in the stratosphere have a greater tilt upstream than indicated by the analysis, which is likely due to the limitations imposed by the relatively coarse dropsonde spacing.

The vertical cross section of the cross-mountain wind speed indicates a maximum of  $54 \text{ m s}^{-1}$  located near 9 km (Fig. 11b), in general agreement with the observed  $48 \text{ m s}^{-1}$  wind speed maximum (Fig. 8b). The strong downslope winds located just above the surface along the lee slope are in excess of  $35 \text{ m s}^{-1}$ , similar to the shooting flow diagnosed from the dropwindsonde data. A region of weak flow is present in the 10–12-km layer coincident with the wave breaking in both simulated and analyzed cross-mountain winds. The region of weak cross-mountain wind speed extends upstream with height in the lower stratosphere similar to other simulations of wave breaking (e.g., Doyle et al. 2000). Weak flow is also present just above the strong downslope winds and coincident with a gravity wave feature that exhibits internal hydraulic jump characteristics similar to those depicted in the analysis based on the dropwindsondes (Fig. 8b). In the upstream region, the dropsondes indicate that stronger vertical shear is present in the 3–9-km layer relative to the simulation.

The simulated wind speed, potential temperature, and TKE derived from the 1.7-km resolution grid mesh was interpolated to a portion of the research aircraft flight transect at the nearest available model output time (1130 UTC 29 January 1997) and is displayed in

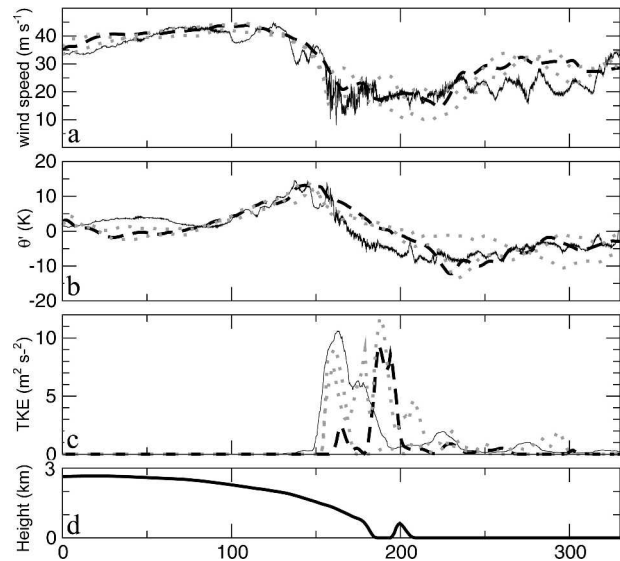


FIG. 12. The NOAA G-IV 25-Hz flight level measurements (solid lines) of the (a) wind speed ( $\text{m s}^{-1}$ ), (b) perturbation potential temperature (K), and (c) turbulence kinetic energy ( $\text{m}^2 \text{s}^{-2}$ ) for a portion of the flight path that extended from central Greenland to 125 km offshore. (d) The terrain interpolated to the flight path. The model-simulated values are interpolated to the flight path from the finest-resolution grid mesh ( $\Delta x = 1.7 \text{ km}$ ) shown by the dashed lines and the model results interpolated to  $0.25^\circ$  north and south of the flight path are shown by the gray dotted lines.

Fig. 12 along with the in situ aircraft observations. To illustrate the spread and variability of the simulated flow in the vicinity of the flight track, the model results interpolated to  $0.25^\circ$  north and south of the flight path are shown by the gray dotted lines in Fig. 12. The perturbation potential temperature is shown for ease of comparison. The highest-resolution grid mesh accurately captures the gross large-scale features of the wave. For example, the model and observations both exhibit a wind speed perturbation of nearly  $30 \text{ m s}^{-1}$  associated with the gravity wave (Fig. 12a) and a potential temperature perturbation greater than  $25 \text{ K}$  (Fig. 12b). Downstream of the highly turbulent region, the observations indicate several wavelike structures in the winds; however, in the model the amplitude of the simulated short wavelength features is substantially weaker. Additionally, the mean wind speed in the simulation downstream of the breaking region is  $2.5$  to  $7.5 \text{ m s}^{-1}$  too large. The model does not reduce the wind speed as much as observed in the strongest portion of the wave breaking; however, this is likely due to a sampling issue as other nearby grid points show larger TKE and weaker wind speeds. The TKE predicted by the model and derived from the 25-Hz research aircraft observations are shown in Fig. 12c. To facilitate a



meaningful comparison between the aircraft observations and the model simulation for the fourth grid mesh ( $\Delta x = 1.7$  km), scales less than 1.7 km are considered turbulence. The model simulated TKE shows two distinct peaks. One maximum occurs in the observed region of minimum wind speed and highest frequency activity, however, the model-simulated TKE maximum of  $2 \text{ m}^2 \text{ s}^{-2}$  is considerably less than the derived TKE maximum of  $10.5 \text{ m}^2 \text{ s}^{-2}$  based on the aircraft data. In the simulation, a second maximum exists 25 km downstream of the initial breaking zone, apparently associated with strong buoyancy and shear contributions. The surrounding grid points just north and south of the flight track indicate considerable variability and appear to match better with the flight level data for the western TKE maximum.

The TKE at 12 km ASL, obtained from the fourth grid mesh (1.7-km horizontal resolution) for 1130 UTC 29 January is shown in Fig. 13a. The simulated TKE indicates a widespread region of wave breaking occurs above the steepest portion of the leeside topography and decays with distance downstream. The cross-mountain wind component at 12 km ASL, shown in Fig. 13b, indicates a strong horizontal gradient in the wind speed is present associated with the wave breaking. For example, the region of wind speed in excess of  $40 \text{ m s}^{-1}$  upstream of the breaking transitions over a relatively short distance of 5–10 km to weak or reversed flow in the downstream. Downstream of the wave breaking, the cross-mountain wind field contains rich structure comprised of streams of weak and strong flow. The source of the weak or reversed flow plumes are linked with the more intense regions of dissipation associated with wave breaking, in contrast to the stronger flow maxima that appear to be associated with regions of relatively weak breaking and dissipation (Fig. 13a), similar to the characteristics of lower-tropospheric gap winds and wakes (e.g., Pan and Smith 1999).

The temporal variability of the wave breaking is illustrated by the time–distance diagram of the cross-mountain wind component at 12 km ASL, shown in Fig. 14. The time section is constructed along a portion of the research aircraft flight path shown in Fig. 13a. The wave breaking is most intense in the 1000–1300 UTC time period, as indicated by the region of TKE in excess of  $10 \text{ m}^2 \text{ s}^{-2}$ . During this time period, the cross-mountain wind speed is a maximum just upstream of the breaking zone, suggestive of an amplifying wave. The wake that forms downstream of the wave breaking, characterized by a region of weak wind speed, expands with time due to advection.

A time–height section of the vertical flux of the horizontal momentum is shown in Fig. 15. The momentum

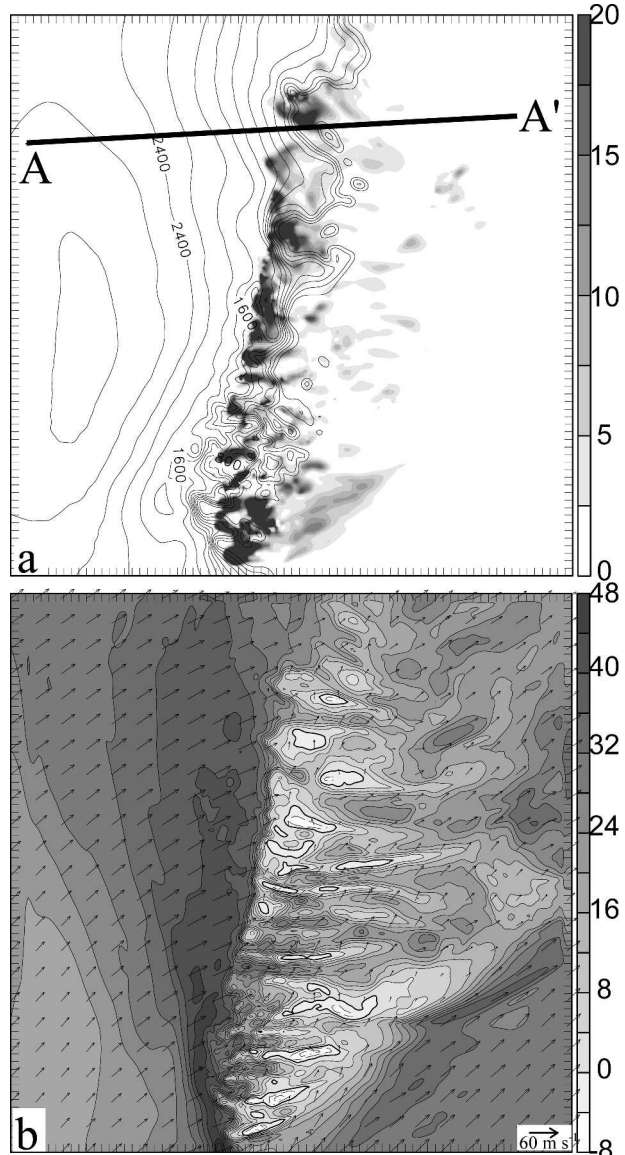


FIG. 13. The model-simulated (a) TKE (grayscale every  $2.5 \text{ m}^2 \text{ s}^{-2}$ ) and (b) wind vectors and cross-mountain wind component (grayscale every  $4 \text{ m s}^{-1}$ ) valid at 1130 UTC 29 Jan 1997 (11.5-h simulation time) at 12 km ASL for the finest-resolution grid mesh ( $\Delta x = 1.7$  km). The model topography is shown in (a) with a 200-m contour interval.

flux is computed as a domain average for the 1.7-km resolution grid mesh and is defined as

$$M_x = \rho \int_{-\infty}^{\infty} u'w' dx dy, \quad (1)$$

where the primes are deviations from the domain average and  $u$  is the cross-mountain wind component. The time–height section indicates that the minimum in

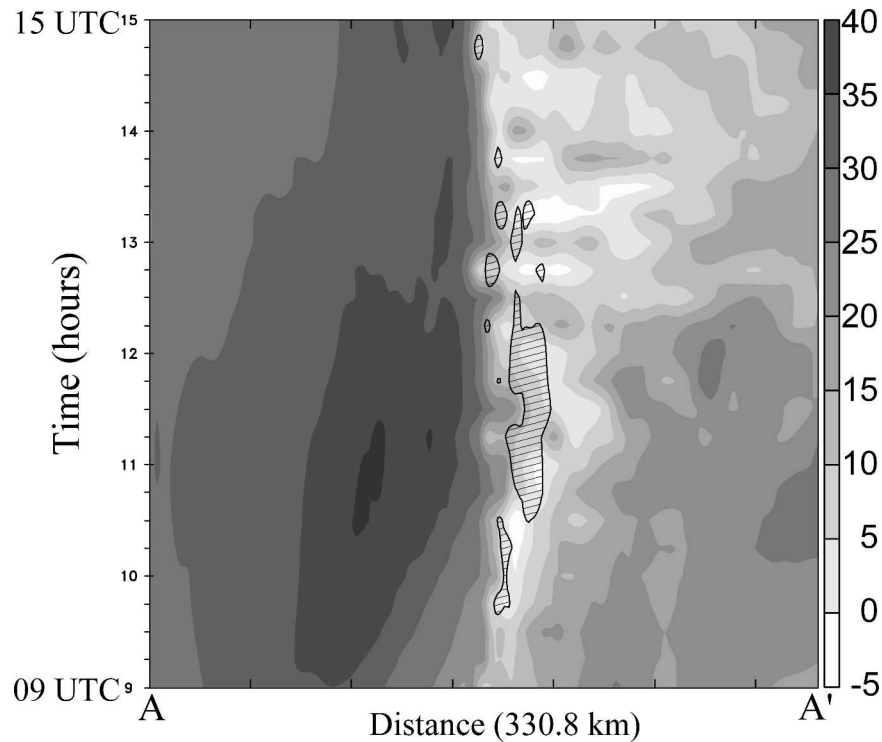


FIG. 14. Time-distance diagram of the model-predicted cross-mountain wind component (grayscale every  $5 \text{ m s}^{-1}$ ) valid from 0900 to 1500 UTC 29 Jan 1997. TKE greater than  $10 \text{ m}^2 \text{ s}^{-2}$  is represented by the hatched regions. The location of the time-distance section is along segment AA' shown in Fig. 13a. The tick marks along the abscissa are shown every 50 km.

the horizontal momentum flux occurs at approximately 9 km ASL between 0800 and 1000 UTC 29 January, coinciding with the wave breaking episode. The horizontal momentum flux minimum occurs in a layer where the vertical shear of the cross-mountain wind component is reversed, which is a situation conducive for breaking (e.g., Smith 1989; Fritts and Alexander 2003). A large vertical gradient in the horizontal momentum flux is present in the lower stratosphere prior to approximately 1400 UTC, which implies momentum deposition in the lower stratosphere. An additional minimum in the wave momentum flux exists in the lower troposphere in the layer between the mountain-top and 4 km ASL. This is likely a manifestation of lower-tropospheric wave breaking along the lee slope. Following the breaking episode, the vertical momentum flux is nearly constant in the troposphere and the flux convergence is reduced in the stratosphere. At the 18-h simulation time, the vertical momentum flux is reduced by nearly an order of magnitude relative to the wave breaking time period and the vertical flux becomes nearly uniform with height, as would be expected from linear theory. The maximum magnitude of

the horizontal momentum flux is approximately  $-1.8 \times 10^{11} \text{ N}$ , or  $-1.5 \text{ N m}^{-2}$  normalized by the area of the finest grid mesh, which compares well with other observations and simulations of gravity waves. For example, Broad (1996) found that the line-averaged meridional component of the vertical flux of horizontal momentum was in the range of  $-1$  to  $-1.5 \text{ N m}^{-2}$  for a lee wave event during the Pyrenees Experiment (PYREX). Beau and Bougeault (1998) found the maximum magnitude of the observed and simulated vertical momentum flux normal to the mean ridge axis to vary between  $0.4$  and  $0.8 \text{ N m}^{-2}$  for other PYREX cases. Hoinka and Clark (1991) simulated flow over the Alps and found an averaged meridional momentum flux in the 5–10 km layer to be  $-2.2 \times 10^{11} \text{ N}$ , which was somewhat larger than observed estimates. Although the observations in the case considered here suggest that the wave breaking event has a significant impact on the flow characteristics for more than 100 km downstream (e.g., Fig. 7), the limited domain precludes a more complete assessment of the scale interactions associated with wave breaking over Greenland and the impact on the larger-scale flow.

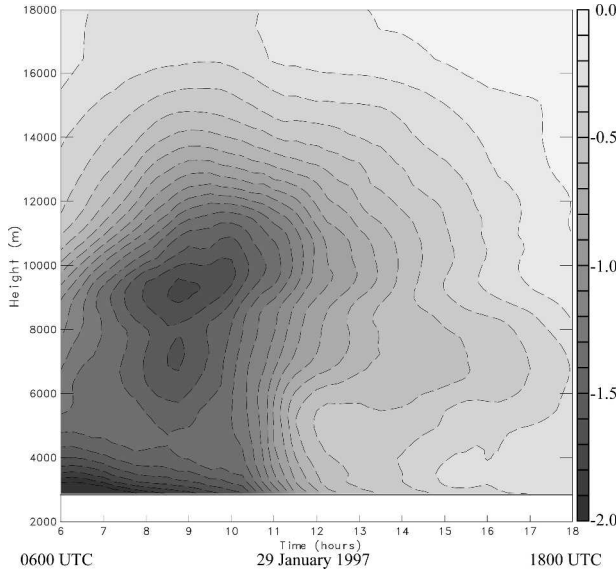


FIG. 15. Time-height diagram of the model-predicted vertical flux of horizontal momentum (grayscale every  $0.1 \times 10^{11}$  N) for the 1.7-km resolution mesh.

#### b. Impact of the Greenland terrain slope on wave breaking

A series of three-dimensional numerical simulations were conducted using the atmospheric portion of COAMPS applied in an idealized configuration in order to explore the sensitivity of wave breaking to the terrain slope. Lilly and Klemp (1979) noted that an asymmetric mountain shape with a gentle upwind slope and a steeper downwind slope tended to generate stronger downslope winds than a symmetric profile for a single layer flow. Miller and Durran (1991) found that the downslope windstorms were most sensitive to terrain asymmetry for two-layer flows. Miller and Durran considered several atmospheric states and noted that for inviscid flows the steepness of the leeside slope has more of an influence on the downslope windstorm than the terrain asymmetry. However, the relationship between the terrain slope and wave breaking for a topographic obstacle similar to the size of Greenland, which may be influenced by rotation and nonlinear effects, is not clear.

The three-dimensional idealized simulations are adiabatic and make use of a free-slip lower boundary condition. Simulations are performed with and without the effects of the earth's rotation. The simulations with rotation are performed with a Coriolis parameter  $f = 1.26 \times 10^{-4} \text{ s}^{-1}$ , corresponding to a  $60^\circ\text{N}$  latitude, consistent with that of Greenland. The simulations are initialized as a horizontally homogeneous initial state with  $N = 0.01 \text{ s}^{-1}$ , that is, hydrostatically balanced and a

zonal wind component  $U = 20 \text{ m s}^{-1}$ . The initial state is in geostrophic balance for the simulations with rotation. The idealized simulations make use of two horizontally nested grid meshes of  $91 \times 91$ , and  $265 \times 265$  points with horizontal grid increments on the computational meshes of 45 and 15 km, respectively. Open lateral boundary conditions are applied for the outermost grid mesh using a constant phase speed approximation. The inner mesh boundary lateral conditions use a one-way interactive nesting technique. The model contains 99 vertical levels on a nonuniform vertical grid consisting of an increment of 200 m in the lowest 10 km, with a gradual increase to 500 m at  $\sim 24$  km and continues with a 500-m increment to the model top at  $\sim 32$  km. A sponge layer of 8-km depth at the model top is used to mitigate spurious reflection of vertically propagating waves.

The topography is specified as a smooth ridge following the basic shape of Epifanio and Durran (2001) with the exception of an additional degree of freedom involving the terrain slope. The long axis is oriented normal to the  $x$  direction and is defined

$$h(x, y) = \begin{cases} \frac{h_m}{16} [1 + \cos(\pi R)]^4, & R \leq 1 \\ 0, & R > 1, \end{cases} \quad (2)$$

where

$$r^2 = \begin{cases} \left(\frac{x}{4a}\right)^2 + \left(\frac{|y| - (\beta - 1)a}{4a}\right)^2, & |y| > (\beta - 1)a \\ \left(\frac{x}{4a}\right)^2, & |y| \leq (\beta - 1)a, \end{cases} \quad (3)$$

and

$$R = c^{1-s} r^s. \quad (4)$$

The slope factor,  $s$ , results in steeper terrain when  $s > 1$  and a more gentle slope for  $s < 1$ , relative to  $s = 1$ . The horizontal aspect ratio,  $\beta$ , is expressed as the ratio of the  $y$  to  $x$  dimension of the ridge. In this formulation for the terrain,  $h(x, y)$  takes the form of a bell-shaped obstacle with length scale  $a$  when  $s = 1$  and maintains a uniform height section through the middle of the ridge when  $\beta > 1$ . Simulations are conducted with constant  $\beta = 4$ ,  $a = 300$  km, and a maximum ridge height,  $h_m$ , of 3000 m. The variable  $c$  is set as a constant value of 0.4.

Vertical cross sections through the ridge centerline ( $h_m = 3000$  m) illustrate the sensitivity of wave breaking to the terrain slope as shown in Fig. 16. In these idealized simulations the model is integrated to 12 hours, which is a reasonable time period to assume steady

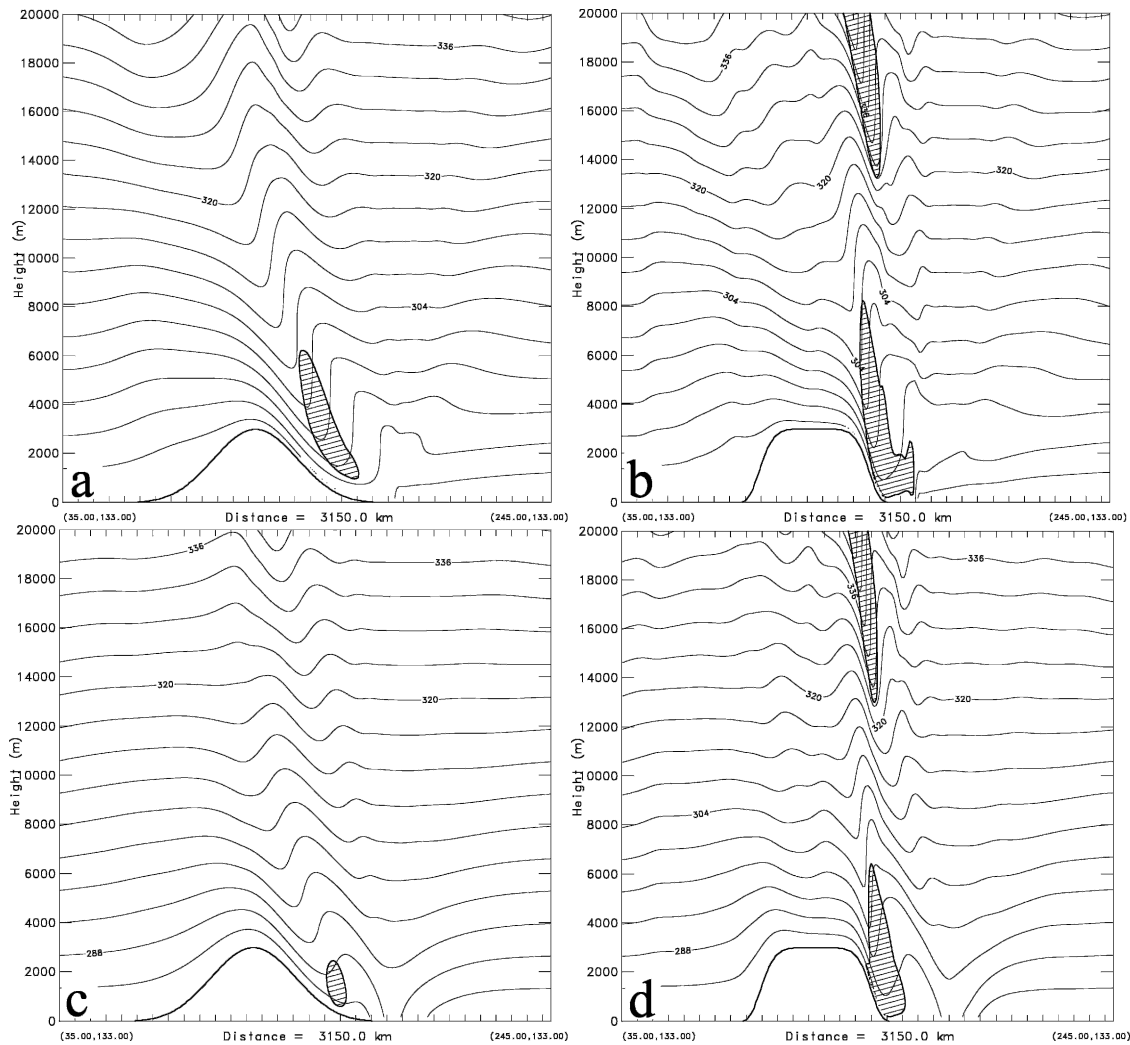


FIG. 16. Vertical sections of potential temperature (K) based on idealized three-dimensional simulations with  $h_m = 3000$  and (a)  $s = 1$  and without rotation, (b)  $s = 3$  and without rotation, (c)  $s = 1$  with rotation ( $f = 1.26 \times 10^{-4} \text{ s}^{-1}$ ), and (d)  $s = 3$  with rotation ( $f = 1.26 \times 10^{-4} \text{ s}^{-1}$ ). The contour interval is 4 K. TKE greater than  $2 \text{ m}^2 \text{ s}^{-2}$  is denoted by the hatched regions; tick marks along the abscissa are shown every 100 km.

synoptic-scale flow. Several simulations conducted using longer integration times indicate that the wave response at 12 hours is similar to that of 24 hours or later, although some differences are apparent in the wave breaking regions. The most intense regions of wave breaking are denoted by hatched areas, which correspond to TKE of  $2 \text{ m}^2 \text{ s}^{-2}$  or greater. The simulation with  $s = 1$  without rotation (Fig. 16a) indicates that a large-amplitude wave is generated in the lee of the bell-shaped terrain. Wave breaking is confined to the lower troposphere below 6 km. The corresponding  $s = 3$  simulation (Fig. 16b) indicates that much stronger and deeper wave breaking is generated by the steeper lee-side terrain, consistent with the results from Lilly and Klemp (1979) and Miller and Durran (1991). Large-

amplitude mountain waves generated by the steep terrain vertically propagate and subsequently amplify and break in the upper levels above 14 km. The inclusion of rotation significantly decreases the wave amplitude for the  $s = 1$  terrain (Fig. 16c), similar to the results of Ólafsson and Bougeault (1997), particularly for the portion of the ridge south of the centerline. The wave breaking generated by the steeper terrain (Fig. 16d) appears to be less sensitive to rotational effects. The steeper terrain essentially has an effective Rossby number,  $Ro = U/fa$ , that is increased relative to the bell-shaped terrain because of the narrow width of the plateau slopes. For example,  $Ro \sim 0.5$  for the  $s = 1$  terrain (Fig. 16c), in contrast to the  $s = 3$  terrain (Fig. 16d), which has an effective  $Ro \sim 1.5$ .



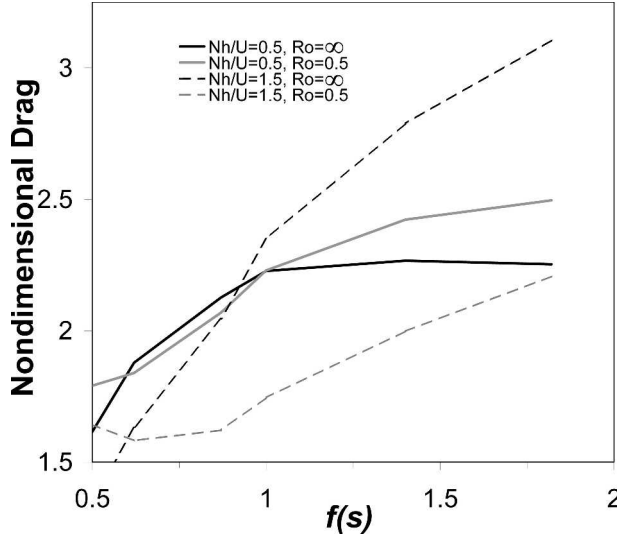


FIG. 17. Simulated nondimensional cross-mountain pressure drag as a function of the normalized terrain slope  $f(s)$ , as defined by Eq. (5). The drag is normalized by the two-dimensional linear drag.

The cross-mountain pressure drag,  $D$ , defined as

$$D = \int_{-\infty}^{\infty} \int_{-\infty}^{\infty} p'(x, y) \frac{\partial h}{\partial x} dx dy,$$

where  $p'$  is the perturbation pressure, was computed for several simulations using various values of  $s$  (0.75, 1.0, 1.5, 2.0, 3.0, and 4.0),  $a = 300$  km, and  $h_m = 1000$  and 3000 m, which correspond to  $Nh_m/U = 0.5$  and 1.5, respectively. The leeside mean slope,  $\bar{S}$ , can be defined as

$$\bar{S} = \frac{(b_1 - b_2)}{d} \left( \frac{h_m}{a} \right) = f(s) \left( \frac{h_m}{a} \right), \quad (5)$$

where  $b_1$  and  $b_2$  are the normalized endpoints over which the slope is computed, in this case 0.8 and 0.2, respectively, and  $d$  represents the normalized horizontal distance between the endpoints corresponding to 80% and 20% of the maximum mountain height. Several integrations were conducted beyond 12 hours and indicate that, although a steady state does not strictly occur, the pressure drag at 12 hours is similar to that obtained at 24 hours and later. The nondimensional pressure drag is shown in Fig. 17 for various normalized slopes  $[f(s)]$  as defined by (5). The drag is normalized by the linear solution for flow over a two-dimensional Witch of Agnesi mountain of height  $h_m$  and length  $L_y$ , in which case  $D_l = \pi \rho_0 U N h_m^2 L_y / 4$ , where  $\rho_0$  is the density at the surface. The pressure drag exhibits more sensitivity to the terrain slope for  $Nh_m/U = 0.5$  than for  $Nh_m/U = 1.5$ . The drag becomes saturated beyond  $f(s)$

$> 1$  for  $Nh_m/U = 1.5$ , likely because the obstacle is of sufficient nondimensional height to force wave breaking regardless of the slope. The pressure drag is reduced by the effect of rotation for  $Nh_m/U = 0.5$  and increased by rotation for  $Nh_m/U = 1.5$ , a result consistent with Ólafsson and Bougeault (1997) and Ólafsson (2000).

## 5. Impact of diabatic cooling on wave amplitude

The ice-covered surface of Greenland undoubtedly has an important influence on the near-surface energy balance and boundary layer response (e.g., Oerlemans and Vugts 1993). The stable boundary layer evident in the soundings (Fig. 6) and dropwindsondes (Fig. 8) for 29 January 1997 is likely a manifestation of airmass cooling over the relatively colder ice sheet through radiation and surface flux processes. The influence of diabatic cooling/heating within the boundary layer on mountain waves has been suggested to be important based on observational and theoretical evidence. Several observational studies of downslope wind frequency indicate that windstorms near Boulder, Colorado, in the lee of the Front Range tend to be more frequent at night and a minimum during the daytime (Brinkmann 1974; Whiteman and Whiteman 1974). Raymond (1972) solved a nonadiabatic form of Long's equation and found that boundary layer cooling over a mountain ridge contributes to an increase in the wave amplitude and boundary layer heating has the opposite impact.

To examine the sensitivity of wave amplitude to diabatic processes in the boundary layer, we examine the response of airflow over an obstacle in the presence of a heating/cooling source within the boundary layer in the small-perturbation limit. We extend the three-layer linear model of Smith et al. (2002) to include a boundary layer heating/cooling diabatic source near the surface. Consider a flow with constant mean wind, a constant buoyancy frequency, and a steady cooling or heating rate, the linear wave equation can be written as

$$\begin{aligned} & \left( U \frac{\partial}{\partial x} + V \frac{\partial}{\partial y} \right)^3 (\nabla^2 \eta) + N^2 \left( U \frac{\partial}{\partial x} + V \frac{\partial}{\partial y} \right) (\nabla_H^2 \eta) \\ & = \frac{g}{C_p \bar{T}} \nabla_H^2 H(x, y, z), \end{aligned} \quad (6)$$

where the local heating rate  $H(x, y, z)$ , which can be expressed in units of energy per unit mass per unit time (i.e.,  $\text{W kg}^{-1}$ ),  $\eta$  is the vertical displacement, and  $\bar{T}$  is the mean temperature. If we assume a heating source exists within the boundary layer at a level  $z = z_H$ ; that is,

$$H(x, y, z) = Qq(x, y)\delta(z - z_H), \quad (7)$$

where  $-1 < q(x, y) < 1$  is a nondimensional heating distribution function and  $Q$  is the strength of the heat source. The wave equation can be solved for  $z < z_H$  and  $z > z_H$  separately with the following matching conditions valid at  $z = z_H$ ,

$$\Delta\eta = 0, \quad (8)$$

$$\left( U \frac{\partial}{\partial x} + V \frac{\partial}{\partial y} \right)^3 \Delta\eta_z = \frac{Qg}{C_p \bar{T}} \nabla_H^2 q(x, y, z), \quad (9)$$

where the horizontal variation of  $\bar{T}$  is ignored. At  $z = 0$ , the boundary condition is  $\eta = h(x, y)$ , where  $h$  is the terrain height.

Applying a Fourier transform in  $(x, y)$  to the adiabatic version of the wave equation (6) using

$$\eta(x, y) = \iint \hat{\eta}(k, l)(z) e^{i(kx + ly)} dk dl \quad (10)$$

for  $z \neq z_H$ , we obtain

$$[\sigma^3(k^2 + l^2 - \partial_{zz}) - N^2\sigma(k^2 + l^2)]\hat{\eta} = 0, \quad (11)$$

where  $\sigma = Uk + Vl$ , and  $\hat{\eta}$  is the transform of  $\eta$ .

The nonhydrostatic solutions to (11) below and above the heating source can be written as

$$\hat{\eta}_l = A_0 e^{im_1 z} + B_0 e^{-im_1 z}, \quad (12)$$

$$\hat{\eta}_u = A e^{im_1 z} + B e^{-im_1 z}, \quad (13)$$

where  $\hat{\eta}_l$  and  $\hat{\eta}_u$  are the solutions below and above the thin heating layer, and  $m_1$  is the vertical wavenumber, defined as  $m_1 = -(k^2 + l^2)(\sigma^2 - N^2)/\sigma^2$  and a sign consistent with  $\text{sgn}(\sigma)$ .

The lower boundary and matching conditions are

$$A_0 + B_0 = \hat{h}, \quad (14)$$

$$A_0 e^{im_1 z_H} + B_0 e^{-im_1 z_H} = A e^{im_1 z_H} + B e^{-im_1 z_H}, \quad (15)$$

$$(A_0 e^{im_1 z_H} - B_0 e^{-im_1 z_H}) - (A e^{im_1 z_H} - B e^{-im_1 z_H}) = \frac{gQ(k^2 + l^2)\hat{q}(k, l)}{C_p \bar{T} m_1 \sigma^3}, \quad (16)$$

where  $z_H$  is the height of the elevated heating source and  $\hat{q}(k, l)$  is the Fourier transform of the source function  $q(x, y)$ . Solving for  $A$  and  $B$ , one obtains

$$A + B = \hat{h} + \frac{gQ(k^2 + l^2)\hat{q}(k, l)}{2C_p \bar{T} m_1 \sigma^3} (e^{im_1 z_H} - e^{-im_1 z_H}). \quad (17)$$

From (17) we note that the linear response of flow

above the heating source can be predicted using an equivalent mountain height. Also, if the surface-based heating layer is infinitesimally thin, there is no influence on the solution. A radiation boundary condition aloft is applied in the top layer, which implies that  $B = 0$  since all three layers contain an identical background state in this application.

For a heated boundary layer with a depth,  $D$ , and a constant heat flux divergence,  $Q$ , the equivalent mountain height is

$$h_e = h + \frac{gQ(k^2 + l^2)\hat{q}(k, l)}{2C_p \bar{T} m_1 \sigma_1^3} \int_0^D (e^{im_1 z} - e^{-im_1 z}) dz, \quad (18)$$

or simplifying further we obtain

$$h_e = \hat{h} - \frac{igQ(k^2 + l^2)\hat{q}(k, l)}{C_p \bar{T} m_1^2 \sigma_1^3} (e^{im_1 D} + e^{-im_1 D} - 1). \quad (19)$$

It follows that the surface cooling/heating is accounted for by applying the equivalent mountain height defined by (19) and solving using the fast Fourier transform method in the three-layer framework of Smith et al. (2002).

The linear solution obtained using the method above is shown in Figs. 18a,b for a two-dimensional flow over a bell-shaped mountain with  $h_m = 1000$  m,  $a = 300$  km,  $N = 0.01$ , and  $U = 15$  m s<sup>-1</sup>. In this case, the surface cooling distribution is specified as

$$q(x) = (1 + x^2 a^{-2})^{-1} - \pi a/L, \quad (20)$$

where  $a = 300$  km, and  $L$  is the domain length. The second term corresponds to a uniformly distributed warming that balances the localized cooling and satisfies the steady state solution condition; that is,  $\int q(x) dx = 0$  over the domain (Smith and Lin 1982; Bretherton 1988). The linear solution without surface heating/cooling, shown in Fig. 18a, exhibits a vertically propagating hydrostatic mountain wave. A second linear solution is obtained assuming  $Q = -0.2$  and a boundary layer depth of 1000 m, implying a  $-200$  W m<sup>-2</sup> flux divergence in the layer. The diabatic cooling along the mountain surface is complex and comprises phase and amplitude information [e.g., (19)]. For the parameters considered in this example, the surface-based diabatic cooling constructively interferes with the mountain contribution, resulting in a 15%–20% increase in the wave amplitude. These results were qualitatively confirmed through a series of two-dimensional simulations using COAMPS (not shown). The ground temperature was initialized 20°C colder than the lowest model level

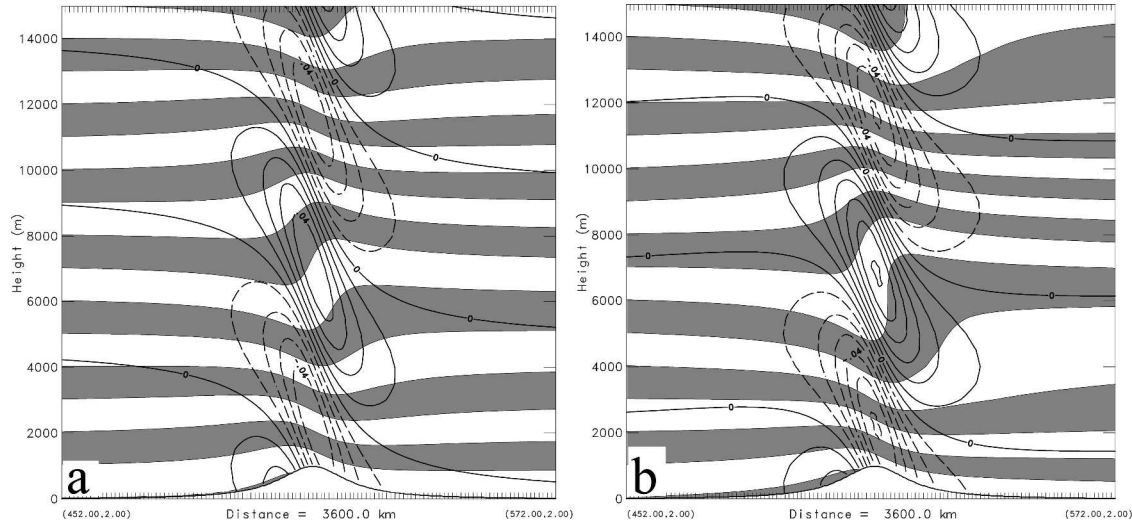


FIG. 18. Vertical cross section of the parcel displacement field (gray shading every 1 km) from linear theory with  $h_m = 1000$  m and  $a = 300$  km for (a) adiabatic flow and (b) diabatic flow with  $Q = -0.2$  for a 1-km boundary layer depth. The vertical velocity is shown at an interval of  $0.01 \text{ m s}^{-1}$ .

air temperature over the mountain surface. The model was integrated to a quasi-steady state at 36 hours. The stratospheric wave breaking in a simulation with surface cooling and  $a = 300$  km was spatially more extensive and achieved greater intensity as quantified by the TKE associated with the breaking layers. Boundary layer cooling has a considerably smaller impact for a narrow mountain because the time scale for air parcels to cross the ridge is smaller and the airstream deflection is reduced. For example, boundary layer cooling has a minimal impact on the airflow for a linear solution obtained with  $a = 10$  km (not shown).

## 6. Summary and conclusions

A large-amplitude mountain wave event was observed during FASTEX on 29 January 1997 by several different observing systems including the NOAA G-IV research aircraft equipped with continuous flight level instrumentation and GPS dropwindsondes. The synoptic scale was characterized by deep southwesterly flow over Greenland with the strongest cross-mountain wind speeds located over the southern portion. Surface wind speeds derived from SSM/I indicated the presence of a large region of weak winds in the lee likely associated with an internal hydraulic jump and wave breaking. Radiosondes and dropwindsondes indicated that strong low-level flow was forced to ascend the Greenland ice sheet and was characterized by a several kilometer deep layer of strong static stability in the lower troposphere positioned beneath a weaker stability layer in the upper troposphere, which was conducive for moun-

tain wave generation. Linear theory and idealized non-linear numerical simulations suggest that boundary layer cooling acts to increase the effective mountain height for relatively wide obstacles such as Greenland, which enhances the wave amplitude and increases the potential for wave breaking.

The evolution and characteristics of the large-amplitude mountain wave event generated by flow over Greenland was documented through the use of in situ measurements and GPS dropwindsondes deployed from the research aircraft. A large-amplitude gravity wave signature with a horizontal scale of approximately 200 km was evident in the velocity and potential temperature in situ measurements, with an  $\sim 25$  K potential temperature and  $\sim 10 \text{ m s}^{-1}$  vertical velocity perturbations associated with the gravity wave. The 50-km spaced dropwindsondes and flight level data depict a large-amplitude wave that deformed the tropopause and lower stratosphere in the 5–12-km layer. One of the dropsondes measured an  $\sim 2$  km deep convectively unstable layer, suggestive of wave breaking. Near the surface, wind speeds were approximately  $30 \text{ m s}^{-1}$  in the lee that transitioned to weaker flow downstream of an internal hydraulic jump feature. The horizontal location of the overturning layer was well correlated with large turbulence values derived from the in situ measurements. The TKE components based on the zonal, meridional, and vertical wind perturbations derived from the flight level data are of comparable magnitude, indicative of quasi-isotropic turbulence. The momentum fluxes associated with the turbulence-scale perturbations exhibit vigorous mixing of momentum with

much weaker wave-scale fluxes. The vertical heat flux calculations suggest that turbulence was in a decay phase at the observation time, although other levels of active turbulence production may have existed. Peaks in the power spectrum occurred at  $\sim 10$  km and 1–5-km wavelengths, indicative of vigorous mixing consistent with the deep layer of isentropic overturning.

The large-amplitude wave breaking event was simulated using the nonhydrostatic COAMPS using four nested grids with a finest horizontal resolution of 1.7 km. The simulated gravity wave structure derived from the 5-km resolution mesh contained many common characteristics with observations and analysis of the dropwindsondes including (i) a large-amplitude wave with deformed tropopause, (ii) wave overturning layers, (iii) a near-stagnant cross-mountain wind component in the breaking zone, (iv) strong downslope windstorm near the surface and a low-level internal hydraulic jump, and (v) a local wind speed maximum of  $50 \text{ m s}^{-1}$  at the base of the wave near 9 km ASL. However, the simulation had a smaller amplitude wave than analyzed based on the research aircraft data. The numerical simulation underscores the difficulty in accurately reproducing a large-amplitude wave associated with a flow characterized by a wide range of spatial scales. The 1.7-km resolution inner grid mesh simulation compared well with the research aircraft data with regard to the wave breaking amplitude, location, and timing. For example, the perturbation wind speed of  $30 \text{ m s}^{-1}$  and perturbation potential temperature of 26 K associated with the mountain wave compared well with the research aircraft measurements of  $35 \text{ m s}^{-1}$  and 25 K. A phase error in the TKE maximum was apparent, which may be related to sampling issues within the wave breaking region. The winds and TKE at 12 km, which is the approximate flight level, exhibited rich small-scale structures associated with the wave breaking, with wakelike plumes that extend downstream from the dissipative regions. The simulated wave breaking was quite transient with the duration of the strongest wave overturning occurring over a 2-h period, which corresponds to the period of maximum momentum flux divergence. The observations and real-data numerical simulation both indicate that wave amplification and breaking occurred above the steep leeside slope of Greenland. A series of idealized simulations suggest that the steep terrain slope increases the effective Rossby number of the relatively wide Greenland topography, and as a result the wave characteristics are less sensitive to rotational effects.

The advancement of knowledge and prediction of mountain wave breaking has been limited by a lack of companion observations, which are necessary for

model evaluation and elucidation of the dynamical processes. Gravity wave breaking is considered to be very localized and transient, which presents a challenge for conventional observing systems. The observations, taken from the NOAA G-IV research aircraft during FASTEX on 29 January 1997, included in situ measurements and GPS dropwindsonde data that provided a relatively rare depiction of large-amplitude wave breaking forced by the large-scale topography of Greenland. Although the objective of the research mission was to observe mountain waves generated by Greenland and was inspired by large-scale numerical model forecasts, the in situ and dropwindsonde measurements of the large-amplitude wave breaking near the geographic region of maximum wave activity and within the narrow time window of maximum wave breaking was serendipitous in many respects.

There are a number of outstanding issues regarding gravity wave breaking generated by large-scale topography such as Greenland and the Tibetan Plateau including (i) wave overturning processes and the significance of turbulent mixing including stratospheric–tropospheric exchange issues and polar stratospheric cloud generation; (ii) wave drag for large-scale obstacles, which is only partially resolved in extended-range forecast and climate models; (iii) predictability of clear-air turbulence; (iv) the linkage between low-level wave breaking that result in strong gradients of surface fluxes and air–sea interaction processes; (v) upscale energy transfer from the wave breaking to the planetary scale; (vi) the relationship between wave breaking, downslope windstorms, and thermally forced flows such as katabatic winds; and (vii) the aggregate effect of these microscale and mesoscale processes on the climate system. Future progress in the dynamical processes and prediction of orographic flows, and in particular mountain wave breaking, will require high-resolution numerical models capable of resolving the wave breakdown processes in concert with airborne and remotely sensed observing systems deployed during future field campaigns.

*Acknowledgments.* Support was provided by the Office of Naval Research's Program Element 0601153N, with computing time supported in part by a grant of HPC time from the Department of Defense Major Shared Resource Center, Aberdeen, MD. COAMPS is a registered trademark of the Naval Research Laboratory. Jeff Hawkins of NRL graciously provided the NSCAT and SSM/I data through the support of the Office of Naval Research (PE 060243N) and the Space and Naval Warfare Systems Command, PMW-185 (PE 0603207N). The authors wish to acknowledge Robert



Gall for helpful discussions and contributions to the planning and execution of the NOAA G-IV research flight over Greenland during FASTEX. The authors are grateful for the outstanding support of the NOAA Aircraft Operations Center (AOC) and for providing the platform and measurements. Comments by three anonymous reviewers substantially improved an earlier version of this manuscript.

## REFERENCES

- Aebischer, U., and C. Schär, 1998: Low-level potential vorticity and cyclogenesis to the lee of the Alps. *J. Atmos. Sci.*, **55**, 186–207.
- Bacmeister, J. T., and M. R. Schoeberl, 1989: Breakdown of vertically propagating two-dimensional gravity waves forced by orography. *J. Atmos. Sci.*, **46**, 2109–2134.
- Barker, E., 1992: Design of the Navy's multivariate optimum interpolation analysis system. *Wea. Forecasting*, **7**, 220–231.
- Beau, I., and P. Bougeault, 1998: Assessment of a gravity-wave drag parameterization with PYREX data. *Quart. J. Roy. Meteor. Soc.*, **124**, 1443–1464.
- Bretherton, C., 1988: Group velocity and the linear response of stratified fluids to internal heat or mass sources. *J. Atmos. Sci.*, **45**, 81–93.
- Bretherton, F. P., 1969: Momentum transport by gravity waves. *Quart. J. Roy. Meteor. Soc.*, **95**, 213–243.
- Brinkmann, W. A. R., 1974: Strong downslope windstorms. *Mon. Wea. Rev.*, **102**, 592–602.
- Broad, A., 1996: High-resolution numerical-model integrations to validate gravity-wave drag parameterization schemes: A case study. *Quart. J. Roy. Meteor. Soc.*, **122**, 1625–1653.
- Bromwich, D. H., J. J. Cassano, T. Klein, G. Heinemann, K. M. Hines, K. Steffen, and J. E. Box, 2001: Mesoscale modeling of katabatic winds over Greenland with the polar MM5. *Mon. Wea. Rev.*, **129**, 2290–2309.
- Chan, K. R., and Coauthors, 1993: A case study of the mountain lee wave event of January 6, 1992. *Geophys. Res. Lett.*, **20**, 2551–2554.
- Clark, T. L., and W. R. Peltier, 1984: Critical level reflection and the resonant growth of nonlinear mountain waves. *J. Atmos. Sci.*, **41**, 3122–3134.
- , W. D. Hall, R. M. Kerr, D. Middleton, L. Radke, F. M. Ralph, P. J. Neiman, and D. Levinson, 2000: Origins of aircraft-damaging clear-air turbulence during the 9 December 1992 Colorado downslope windstorm: Numerical simulations and comparison with observations. *J. Atmos. Sci.*, **57**, 1105–1131.
- Dolgushin, L. D., and G. B. Osipova, 1989: *Glaciers*. Publishing House Mysl, 444 pp.
- Dörnbrack, A., 1998: Turbulent mixing by breaking gravity waves. *J. Fluid Mech.*, **375**, 113–141.
- , and T. Dürbeck, 1998: Turbulent dispersion of aircraft exhausts in regions of breaking gravity waves. *Atmos. Environ.*, **32**, 3105–3112.
- Doyle, J. D., and M. A. Shapiro, 1999: Flow response to large-scale topography: The Greenland tip jet. *Tellus*, **51A**, 728–748.
- , and R. B. Smith, 2003: Mountain waves over the Hohe Tauern. *Quart. J. Roy. Meteor. Soc.*, **129**, 799–823.
- , and Coauthors, 2000: An intercomparison of model-predicted wave breaking for the 11 January 1972 Boulder windstorm. *Mon. Wea. Rev.*, **128**, 901–914.
- Durran, D. R., 1986: Another look at downslope windstorms. Part I: The development of analogs to supercritical flow in an infinitely deep, continuously stratified fluid. *J. Atmos. Sci.*, **43**, 2527–2543.
- Epifanio, C. C., and D. R. Durran, 2001: Three-dimensional effects in high-drag-state flows over long ridges. *J. Atmos. Sci.*, **58**, 1051–1065.
- Fritts, D. C., and M. J. Alexander, 2003: Gravity wave dynamics and effects in the middle atmosphere. *Rev. Geophys.*, **41**, 1003, doi:10.1029/2001RG000106.
- , J. F. Gartin, and Ø. Andreassen, 1996: Wave breaking and transition to turbulence in stratified shear flows. *J. Atmos. Sci.*, **53**, 1057–1085.
- Grose, W. L., and B. J. Hoskins, 1979: On the influence of orography on large-scale atmospheric flow. *J. Atmos. Sci.*, **36**, 223–234.
- Harshvardhan, R. Davies, D. Randall, and T. Corsetti, 1987: A fast radiation parameterization for atmospheric circulation models. *J. Geophys. Res.*, **92**, 1009–1015.
- Hines, C. O., 1960: Internal atmospheric gravity waves at ionospheric heights. *Can. J. Phys.*, **38**, 1441–1481.
- Hodur, R. M., 1997: The Naval Research Laboratory's Coupled Ocean/Atmosphere Mesoscale Prediction System (COAMPS). *Mon. Wea. Rev.*, **125**, 1414–1430.
- Hoinka, K. P., and T. L. Clark, 1991: Pressure drag and momentum fluxes due to the Alps. I: Comparison between numerical simulations and observations. *Quart. J. Roy. Meteor. Soc.*, **117**, 495–525.
- Jiang, Q., and J. D. Doyle, 2004: Gravity wave breaking over the central Alps: Role of complex terrain. *J. Atmos. Sci.*, **61**, 2249–2266.
- Joly, A., and Coauthors, 1997: The Fronts and Atlantic Storm-Track Experiment (FASTEX): Scientific objectives and experimental design. *Bull. Amer. Meteor. Soc.*, **78**, 1917–1940.
- Kain, J. S., and J. M. Fritsch, 1993: Convective parameterization for mesoscale models: The Kain–Fritsch scheme. *The Representation of Cumulus Convection in Numerical Models, Meteor. Monogr.*, No. 46, Amer. Meteor. Soc., 165–170.
- Klemp, J., and R. Wilhelmson, 1978: The simulation of three-dimensional convective storm dynamics. *J. Atmos. Sci.*, **35**, 1070–1096.
- Lester, P. F., O. Sen, and R. E. Bach, 1989: The use of DFDR information in the analysis of a turbulence incident over Greenland. *Mon. Wea. Rev.*, **117**, 1103–1107.
- Leutbecher, M., and H. Volkert, 2000: The propagation of mountain waves into the stratosphere: Quantitative evaluation of three-dimensional simulations. *J. Atmos. Sci.*, **57**, 3090–3108.
- Lilly, D. K., 1978: A severe downslope windstorm and aircraft turbulence event induced by a mountain wave. *J. Atmos. Sci.*, **35**, 59–77.
- , and E. J. Zipser, 1972: The Front Range windstorm of January 11, 1972. *Weatherwise*, **25**, 56–63.
- , and P. J. Kennedy, 1973: Observations of a stationary mountain wave and its associated momentum flux and energy dissipation. *J. Atmos. Sci.*, **30**, 1135–1152.
- , and J. B. Klemp, 1979: The effects of terrain shape on nonlinear hydrostatic mountain waves. *J. Fluid Mech.*, **95**, 241–261.
- Lindzen, R. S., 1967: Thermally driven diurnal tide in the atmosphere. *Quart. J. Roy. Meteor. Soc.*, **93**, 18–42.

- Louis, J. F., 1979: A parametric model of vertical eddy fluxes in the atmosphere. *Bound.-Layer Meteor.*, **17**, 187–202.
- Miller, P. P., and D. R. Durran, 1991: On the sensitivity of downslope windstorms to the asymmetry of the mountain profile. *J. Atmos. Sci.*, **48**, 1457–1473.
- Murphy, B. F., I. Marsiat, and P. Valdes, 2002: Atmospheric contributions to the surface mass balance of Greenland in the HadAM3 atmospheric model. *J. Geophys. Res.*, **107**, 4556, doi:10.1029/2001JD000389.
- Nastrom, G. D., and K. S. Gage, 1985: A climatology of atmospheric wavenumber spectra of wind and temperature observed by commercial aircraft. *J. Atmos. Sci.*, **42**, 950–960.
- Oerlemans, J., and H. F. Vugts, 1993: A meteorological experiment in the melting zone of the Greenland ice sheet. *Bull. Amer. Meteor. Soc.*, **74**, 355–366.
- Ólafsson, H., 2000: The impact of flow regimes on asymmetry of orographic drag at moderate and low Rossby numbers. *Tellus*, **52A**, 365–379.
- , and P. Bougeault, 1996: Nonlinear flow past an elliptical ridge. *J. Atmos. Sci.*, **53**, 2465–2489.
- , and —, 1997: The effect of rotation and surface friction on orographic drag. *J. Atmos. Sci.*, **54**, 193–210.
- Palmer, T. N., G. J. Shutts, and R. Swinbank, 1986: Alleviation of systematic westerly bias in general circulation and numerical weather prediction models through an orographic gravity wave drag parameterization. *Quart. J. Roy. Meteor. Soc.*, **112**, 1001–1039.
- Pan, F., and R. B. Smith, 1999: Gap winds and wakes: SAR observations and numerical simulations. *J. Atmos. Sci.*, **56**, 905–923.
- Peltier, W. R., and T. L. Clark, 1979: The evolution and stability of finite-amplitude mountain waves. Part II: Surface wave drag and severe downslope windstorms. *J. Atmos. Sci.*, **36**, 1498–1529.
- Petersen, G. N., H. Ólafsson, and J. E. Kristjánsson, 2003: Flow in the lee of idealized mountains and Greenland. *J. Atmos. Sci.*, **60**, 2183–2195.
- Pickart, R. S., M. A. Spall, M. H. Ribergaard, G. W. K. Moore, and R. F. Milliff, 2003: Deep convection in the Irminger Sea forced by the Greenland tip jet. *Nature*, **424**, 152–156.
- Ralph, F. M., P. J. Neiman, and D. Levinson, 1997: Lidar observations of a breaking mountain wave associated with extreme turbulence. *Geophys. Res. Lett.*, **24**, 663–666.
- Raymond, D. J., 1972: Calculation of airflow over an arbitrary ridge including diabatic heating and cooling. *J. Atmos. Sci.*, **29**, 837–843.
- Rutledge, S. A., and P. V. Hobbs, 1983: The mesoscale and microscale structure of organization of clouds and precipitation in midlatitude cyclones. VIII: A model for the “seeder-feeder” process in warm-frontal rainbands. *J. Atmos. Sci.*, **40**, 1185–1206.
- Schär, C., and R. B. Smith, 1993: Shallow-water flow past isolated topography. Part I: Vorticity production and wake formation. *J. Atmos. Sci.*, **50**, 1373–1400.
- Schmid, H., and A. Dörnbrack, 1999: Simulation of breaking gravity waves during the south foehn of 7–13 January 1996. *Beitr. Phys. Atmos.*, **72**, 287–303.
- Schwierz, C. B., and H. C. Davies, 2003: Evolution of a synoptic-scale vortex advecting toward a high mountain. *Tellus*, **55A**, 158–172.
- Shen, B.-W., and Y.-L. Lin, 1999: Effects of critical levels on two-dimensional back-sheared flow over an isolated mountain ridge on an  $f$  plane. *J. Atmos. Sci.*, **56**, 3286–3302.
- Shutts, G., 1992: Observations and numerical model simulations of a partially trapped lee wave over the Welsh mountains. *Mon. Wea. Rev.*, **120**, 2056–2066.
- , 1998: Stationary gravity-wave structure in flows with directional wind shear. *Quart. J. Roy. Meteor. Soc.*, **124**, 1421–1442.
- Smith, R. B., 1985: On severe downslope winds. *J. Atmos. Sci.*, **43**, 2597–2603.
- , 1989: Hydrostatic flow over mountains. *Advances in Geophysics*, Vol. 31, Academic Press, 1–41.
- , and Y.-L. Lin, 1982: The addition of heat to a specified airstream with application to the dynamics of orographic rain. *Quart. J. Roy. Meteor. Soc.*, **108**, 353–378.
- , S. T. Skubis, J. D. Doyle, A. Broad, C. Kiemle, and H. Volkert, 2002: Mountain waves over Mt. Blanc: Influence of a stagnant boundary layer. *J. Atmos. Sci.*, **59**, 2073–2092.
- Smolarkiewicz, P. K., and R. Rotunno, 1989: Low Froude number flow past three-dimensional obstacles. Part I: Baroclinically generated vortices. *J. Atmos. Sci.*, **46**, 1154–1164.
- , L. G. Margolin, and A. A. Wysogrodzi, 2001: A class of nonhydrostatic global models. *J. Atmos. Sci.*, **58**, 349–364.
- Thorpe, A. J., H. Volkert, and D. Heimann, 1993: Potential vorticity of flow along the Alps. *J. Atmos. Sci.*, **50**, 1573–1590.
- VanZandt, T. E., and D. C. Fritts, 1989: A theory of enhanced saturation of the gravity wave spectrum due to increases in atmospheric stability. *Pure Appl. Geophys.*, **130**, 399–420.
- Vosper, S. B., and S. D. Mobbs, 1996: Lee waves over the English Lake District. *Quart. J. Roy. Meteor. Soc.*, **122**, 1283–1305.
- Wei, M.-Y., and T. K. Schaack, 1984: Seasonal distributions of mountain torques during FGGE. *J. Atmos. Sci.*, **41**, 3032–3039.
- Whiteman, C. D., and J. G. Whiteman, 1974: An historical climatology of damaging downslope windstorms at Boulder, Colorado. NOAA Tech. Rep. ERL 336-APCL 35, 62 pp. [Available from the Superintendent of Documents, U.S. Government Printing Office, Washington, DC 20401.]
- Worthington, R. M., 1998: Tropopausal turbulence caused by the breaking of mountain waves. *J. Atmos. Solar-Terr. Phys.*, **60**, 1543–1547.